AIAA SciTech Forum
9 - 13 January 2017, Grapevine, Texas
55th AIAA Aerospace Sciences Meeting

Hyperbolic Navier-Stokes Method for High-Reynolds-Number Boundary-Layer Flows

Hiroaki Nishikawa* and Yi Liu†
National Institute of Aerospace, Hampton, VA 23666

In this paper, we discuss issues and resolutions concerning the hyperbolic Navier-Stokes method for high-Reynolds-number flows. Implicit hyperbolic Navier-Stokes solvers have been found to encounter significant convergence deterioration and robustness issues for high-Reynolds-number boundary layer flows. The problem is examined in details for a one-dimensional advection-diffusion model, and resolutions are discussed. One of the major findings is that the relaxation length scale needs to be inversely proportional to the Reynolds number for boundary layer flows. Accurate, robust, and efficient boundary-layer calculations by hyperbolic schemes are demonstrated for advection-diffusion equations in one and two dimensions, and the Navier-Stokes equations.

I. Introduction

The hyperbolic method is an approach to deriving spatial discretizations of diffusion terms via a hyperbolic formulation [1, 2]. The method has recently been extended to the three-dimensional Navier-Stokes equations [3, 4] towards the development of efficient high-order viscous solvers for practical applications. In this method, viscous discretizations are simplified by formulating the viscous terms as a first-order hyperbolic system and thus allowing inviscid methods to be directly applicable to the viscous terms. The hyperbolic formulations are deliberately constructed so as to preserve the equivalence to the viscous terms in the steady form. As a result, the resulting spatial discretization is always consistent with the original viscous terms expressed in the form of a first-order system. In two dimensions, a hyperbolic viscous system termed HNS14 has been constructed with the viscous stresses and the heat fluxes introduced as additional variables [5, 6], and an extended version termed HNS20 has been proposed in Ref.[7] with the density gradient, the velocity gradients, and the heat fluxes to enable higher-order approximations to the inviscid terms. These hyperbolic viscous systems are discretized by upwind schemes, and added to a conventional inviscid scheme to generate hyperbolic Navier-Stokes (HNS) schemes. The resulting HNS schemes have been shown to bring various key improvements to conventional unstructured-grid solvers, e.g., high-order derivative predictions on unstructured grids. Ref.[3] demonstrates that the three-dimensional version of HNS20 has a complete eigenstructure with linearly independent eigenvectors for the viscous system, and the upwind HNS20 scheme produces high-quality derivatives for three-dimensional viscous flow problems on unstructured grids. Later, Ref.[4] presented verification studies for third-order accuracy in the inviscid term approximation, the high-order derivative prediction capability for various viscous flow problems in three dimensions, and efficient drag predictions over a conventional solver.

During the development towards practical HNS unstructured-grid solvers, however, it has been found that the HNS solvers encounter difficulties for high-Reynolds-number flows involving boundary layers. It has been pointed out [8,9] that the relaxation length scale associated with the HNS formulations needs to be reduced from a standard value of $\frac{1}{2\pi}$ in such flows, or iterative solvers may diverge. To address the issue, Ref.[4] proposed an improved length scale definition as a function of the free stream Reynolds number. Although successful for the test cases presented, the mechanism behind was not completely understood. The objective of this paper is to investigate the issue in details and provide practical resolutions. The problem is examined for a one-dimensional advection-diffusion model, and resolutions are discussed. This study focuses on the edge-based discretization, which has been one of the main target discretization methods in the hyperbolic method [3, 4, 5, 6, 7, 10, 11]. However, the results are relevant

*Associate Research Fellow (hiro@nianet.org), National Institute of Aerospace, 100 Exploration Way, Hampton, VA 23666 USA, Associate Fellow AIAA
†Senior Research Scientist (yi.liu@nianet.org), National Institute of Aerospace, 100 Exploration Way, Hampton, VA 23666 USA, Senior Member AIAA

to other discretization methods, including finite-volume and finite-difference methods. Proposed resolutions are critically assessed for one- and two-dimensional advection diffusion equations, the viscous Burgers equation, and the three-dimensional Navier-Stokes equations.

As it will turn out, the problem can be traced back to a lack of dissipation, or equivalently of high-frequency damping, in a boundary layer. Traditionally, analyses of numerical schemes for boundary layer problems focus on accuracy and dissipative behaviors of advection schemes (see, e.g., Refs.[12,13,14,15]): non-dissipative schemes fail to damp out high-frequency error modes and generate oscillations on under-resolved grids, and upwind schemes provide sufficient damping to suppress the oscillations. The focus on the advection schemes is due to the difficulty of controlling the damping property of the central diffusion scheme. Consider the central scheme for the advection-diffusion equation in one dimension, $a\partial_x u - \nu\partial_{xx} u = 0$:

$$a\frac{u_{j+1} - u_{j-1}}{h} - \nu\frac{u_{j+1} - 2u_j + u_{j-1}}{h^2} = 0, \tag{I.1}$$

where a and ν are positive constants, and h is the mesh spacing of a uniform grid. This scheme can be written in the conservative form, $f_{j+1/2} - f_{j-1/2} = 0$, with the numerical flux [16],

$$f_{j+1/2} = \frac{1}{2}(f_{j+1} + f_j) - \frac{a}{Re_h}(u_R - u_L), \tag{I.2}$$

where $Re_h = ah/\nu$, $f_j = au_j - \nu(u_{j+1} - u_{j-1})/(2h)$, $f_{j+1} = au_{j+1} - \nu(u_{j+2} - u_j)/(2h)$, $u_L = u_j + (u_{j+1} - u_{j-1})/4$, and $u_R = u_{j+1} + (u_{j+2} - u_j)/4$. The second term provides the high-frequency damping, but it will be reduced for large-Re_h grids, where the damping effect is critically important for eliminating unresolved high-frequency modes. The well-known mesh-Reynolds-number restriction for this scheme, $Re_h \leq 2$, implies that the damping coefficient needs to be retained such that $a/Re_h \geq a/2$; the lower bound corresponds to the dissipation coefficient from the upwind advection scheme. Therefore, the restriction can be easily removed by the use of upwind schemes for advection, totally avoiding a practically difficult task of generating grids with $Re_h \leq 2$. In hyperbolic advection-diffusion schemes, the dissipation matrix of hyperbolic diffusion schemes diminishes for high-Reynolds numbers as will be shown later, but it cannot be compensated by upwind advection schemes. This is because a scalar dissipation term from upwind advection schemes cannot recover the full dissipation matrix of hyperbolic diffusion schemes. Analysis should, therefore, directly address the damping property of hyperbolic diffusion schemes. In this paper, however, instead of directly tackling the dissipation issue, we approach the problem by investigating accuracy with the classical modal analysis [14]. For a first-order hyperbolic advection-diffusion scheme, we derive an optimal length scale that minimizes the first-order error, and then show that it will prevent the dissipation coefficient from vanishing for high Reynolds numbers. Fourier analyses will be performed to confirm that the optimal length scale resolves issues in iterative solvers also.

In the hyperbolic method, two different constructions have been proposed: Scheme-I and Scheme-II [10, 11]. Scheme-I is a straightforward discretization of the hyperbolic formulation. Scheme-II is a more efficient construction, where the gradient variables are used directly to construct a high-order reconstruction of the solution variables and upgrade the order of approximation in inviscid terms [3]. An improved variant of Scheme-I, termed Scheme-IQ, has been proposed in Ref.[4] as a practical alternative to Scheme-II; it uses the gradient variables indirectly to construct higher-order gradients and achieve the same inviscid scheme improvement as Scheme-II. In this paper, these schemes are examined for boundary layer problems. It will be shown that Scheme-I and Scheme-IQ can be made robust and accurate for boundary-layer calculations, but Scheme-II is subject to a serious mesh-Reynolds-number restriction, and can easily fail for high-Reynolds-number boundary-layer problems.

The optimal length scale derived for the first-order scheme will be extended to second-order schemes, the viscous Burgers equation, and the compressible Navier-Stokes equations. A correction factor will be derived by minimizing the number of negative roots in the modal analysis of a second-order scheme. Numerical experiments show that the second-order correction is essential to obtain accurate solutions on under-resolved grids. Extensions to nonlinear equations require the length scale to be dependent on the local solution, but free stream evaluations also provide practical approximations. The formula proposed in Ref.[4] has been found to be effective also, and seemingly related to the correction factor mentioned above.

The paper is organized as follows. In Section II, the target discretization and solver are described. In Section III, issues and resolutions are discussed in details for a linear advection-diffusion equation. In Section IV, extensions to the viscous Burgers are discussed. In Section, V, extensions to the compressible Navier-Stokes system are discussed. In Section VI, numerical results are presented. Section VII, concludes the paper with remarks and a summary of findings.

II. Target Model System, Discretization, and Solver

II.A. Target Model System

Consider a steady advection-diffusion equation in one dimension:

$$\partial_x(f^a + f^d) = 0, \tag{II.1}$$

where f^a and f^d denote the advective and diffusive fluxes, respectively:

$$f^a = f^a(u), \quad f^d = \nu\,\partial_x u. \tag{II.2}$$

In this study, we assume that the diffusion coefficient ν is a positive constant, but allow the advective characteristic speed $a(u) = \partial f^a/\partial u$ to be negative. Solutions are sought in the domain $x \in [0, 1]$ with two boundary conditions $u(0) = 0$ and $u(1) = U_\infty$, where U_∞ is a given constant. In the hyperbolic method, the steady advection-diffusion equation is reformulated as a first-order system of the form:

$$\partial_\tau u + \partial_x f^a = \partial_x p, \quad \partial_\tau p = \frac{\nu}{T_r}\left(\partial_x u - \frac{p}{\nu}\right), \tag{II.3}$$

where τ is a pseudo time variable. The first-order system is hyperbolic in τ as proved in Ref.[2]. The parameter T_r, which is called the relaxation time, is a free parameter that can be determined to accelerate convergence to the pseudo steady state [1, 2]. For the target discretization considered here, it is defined as [10, 11]

$$T_r = \frac{L_r^2}{\nu}, \tag{II.4}$$

where L_r is a relaxation length scale, which has been determined in Ref.[10] to maximize error propagation effects as

$$L_r = \frac{1}{2\pi}. \tag{II.5}$$

This value appears also as the leading term of an optimal formula derived for a hyperbolic residual-distribution scheme for diffusion [1]. It may be considered as an optimal leading formula for general diffusion schemes, and for this reason, we specifically denote

$$L_d \equiv \frac{1}{2\pi}, \tag{II.6}$$

which will be referred to as the diffusion length scale to emphasize that it is targeted for pure diffusion problems. The target system (II.3) is written in the vector form as

$$\mathbf{P}^{-1}\partial_\tau \mathbf{u} + \partial_x \mathbf{f} = \mathbf{s}, \tag{II.7}$$

where

$$\mathbf{P}^{-1} = \begin{bmatrix} 1 & 0 \\ 0 & T_r/\nu \end{bmatrix}, \mathbf{u} = \begin{bmatrix} u \\ p \end{bmatrix}, \mathbf{f} = \mathbf{f}^a + \mathbf{f}^d = \begin{bmatrix} f^a(u) \\ 0 \end{bmatrix} + \begin{bmatrix} -p \\ -u \end{bmatrix} = \begin{bmatrix} f^a(u) - p \\ -u \end{bmatrix}, \mathbf{s} = \begin{bmatrix} 0 \\ -p/\nu \end{bmatrix}. \tag{II.8}$$

Note that the hyperbolic system formulation (II.7) is a nonlinear-type formulation applicable to variable viscosities introduced for the Navier-Stokes equations in Ref.[5]. It is important to note that the system (II.7) is equivalent to the steady advection-diffusion equation (II.1) when $\partial_\tau \mathbf{u} = 0$: either integrate the system to a pseudo-steady state or simply drop the pseudo-time derivative. The steady equivalence implies that a spatial discretization of the system is consistent with the original steady advection-diffusion equation (II.1). In this sense, the hyperbolic method can be considered as an approach to deriving a consistent spatial discretization for diffusion terms.

II.B. Target Discretization

II.B.1. Node-Centered Edge-Based Discretization

The main target discretization method is a node-centered edge-based method [3, 5, 6, 7, 10, 11], which defines the residual at an interior node j on a one-dimensional grid $[x_0 = 0, x_1, x_2, \cdots, x_N = 1]$ as

$$\mathbf{Res}_j = -\mathbf{P}_j\left(\frac{\Phi_{j+1/2} - \Phi_{j-1/2}}{\Delta x_j} + \mathbf{s}_j\right), \quad j = 1, 2, \cdots, N-1, \tag{II.9}$$

where Φ denotes a numerical flux and $\Delta x_j = (x_{j+1} - x_{j-1})/2$ is the dual control volume around the node j. The residuals at boundary nodes will be discussed later in Section II.B.4. Note that the pseudo time derivative has been dropped, and thus the residual above is a consistent approximation to the steady advection-diffusion equation (II.1). The numerical flux Φ is a function of left and right states $\mathbf{u}_L$ and $\mathbf{u}_R$:

$$\Phi(\mathbf{u}_L, \mathbf{u}_R) = \frac{1}{2}\left(\mathbf{f}_L + \mathbf{f}_R\right) - \frac{1}{2}\mathbf{Q}\left(\mathbf{u}_R - \mathbf{u}_L\right), \tag{II.10}$$

where $\mathbf{Q}$ is a dissipation matrix. The left and right states are defined at the interface as will be discussed later. It is straightforward to construct an upwind dissipation matrix for the hyperbolic advection-diffusion system by using the eigen-structure of the system (see Appendix C). However, this unified approach is not applicable to the compressible Navier-Stokes equations because the eigen-structure of the hyperbolic NS system has not been found yet. To enable extensions to the compressible NS system, a simplified approach has been introduced in Ref.[5], where the numerical flux is constructed separately for inviscid and viscous terms. For the advection-diffusion equation, it leads to the following dissipation matrix (see Ref.[11]):

$$\mathbf{Q} = \begin{bmatrix} |a| + a_v & 0 \\ \\ 0 & T_r a_v/\nu \end{bmatrix}, \tag{II.11}$$

where a_v is the wave speed associated with the pure hyperbolic diffusion system [10]:

$$a_v = \sqrt{\frac{\nu}{T_r}} = \frac{\nu}{L_r}. \tag{II.12}$$

For a nonlinear case, the advective wave speed a depends on the solution, and an eigenvalue smoothing technique [17] is used to avoid vanishing diagonals in the residual Jacobian:

$$|a| \to \frac{1}{2}\left(\frac{|a|^2}{\delta} + \delta\right), \quad \delta = 0.25, \tag{II.13}$$

or implicit iterative solvers will fail.

The main subject of the present work is the investigation of issues associated with the simplified approach used to define the dissipation matrix as in Equation (II.11). As will be demonstrated later, similar issues are not encountered if the dissipation matrix is constructed based on the unified hyperbolic advection-diffusion system.

II.B.2. Second-Order Schemes

For second-order accuracy, the left and right states are computed, for example at the face $j + 1/2$, by

$$\mathbf{u}_L = \mathbf{u}_j + \frac{\Delta x_j}{2}(\partial_x \mathbf{u})_j, \quad \mathbf{u}_R = \mathbf{u}_{j+1} - \frac{\Delta x_{j+1}}{2}(\partial_x \mathbf{u})_{j+1}, \tag{II.14}$$

where $(\partial_x \mathbf{u})_j$ denotes the solution gradient at j computed by a linear least-squares (LSQ) method over a set $\{k_j\}$ of neighbors of j:

$$(\partial_x \mathbf{u})_j = \frac{\displaystyle\sum_{k \in \{k_j\}} (\mathbf{u}_k - \mathbf{u}_j)(x_k - x_j)}{\displaystyle\sum_{k \in \{k_j\}} (x_k - x_j)^2}, \tag{II.15}$$

where $\{k_0\} = \{1, 2\}$, $\{k_N\} = \{N-2, N-1\}$, and $\{k_j\} = \{j-1, j+1\}$ for $0 < j < N$. Similarly, the left and right fluxes are computed as

$$\mathbf{f}_L = \mathbf{f}_j + \frac{\Delta x_j}{2}\left(\frac{\partial \mathbf{f}}{\partial \mathbf{u}}\right)(\partial_x \mathbf{u})_j, \quad \mathbf{f}_R = \mathbf{f}_{j+1} - \frac{\Delta x_{j+1}}{2}\left(\frac{\partial \mathbf{f}}{\partial \mathbf{u}}\right)(\partial_x \mathbf{u})_{j+1}, \tag{II.16}$$

which are equivalent to $\mathbf{f}_L = \mathbf{f}(\mathbf{u}_L)$ and $\mathbf{f}_R = \mathbf{f}(\mathbf{u}_R)$, respectively, for linear equations. The resulting scheme is called Scheme-I [10], and achieves second-order accuracy for both u and p on irregularly-spaced grids. An economical version, called Scheme-II [10], is obtained by replacing $(\partial_x u)_j$ by p_j/ν:

$$u_L = u_j + \frac{\Delta x_j}{2}\frac{p_j}{\nu}, \quad u_R = u_{j+1} - \frac{\Delta x_{j+1}}{2}\frac{p_{j+1}}{\nu}. \tag{II.17}$$

This scheme is more economical for two reasons. First, it does not require gradient computations for the primal variable u. Second, it gives higher-order accuracy in the advective term. The node-centered scheme considered here is known to achieve third-order accuracy if the gradient is computed with second-order accuracy, and in nonlinear cases, the flux is linearly extrapolated for nonlinear cases [18]. This is exactly the case with Scheme-II because the gradient variable p is obtained with second-order accuracy. In contrast, Scheme-I gives also second-order accurate p, but uses first-order accurate gradients, $(\partial_x \mathbf{u})_j$, in the linear solution reconstruction. Scheme-IQ, which is a modified version of Scheme-I that achieves higher-order accuracy in the advective term [4], will be described later in Section III.C.

II.B.3. First-Order Schemes

For analyses and implicit solver constructions, we consider first-order accurate versions of Scheme-I and Scheme-II, which are defined by zero LSQ gradients. That is, the first-order version of Scheme-I is defined by

$$\begin{aligned} u_L &= u_j, \qquad & p_L &= p_j, \\ u_R &= u_{j+1}, \qquad & p_R &= p_{j+1}. \end{aligned} \tag{II.18}$$

and the first-order version of Scheme-II by

$$\begin{aligned} u_L &= u_j + \frac{\Delta x_j}{2}\left(\frac{p_j}{\nu}\right), & p_L &= p_j, \\ u_R &= u_{j+1} - \frac{\Delta x_{j+1}}{2}\left(\frac{p_{j+1}}{\nu}\right), & p_R &= p_{j+1}. \end{aligned} \tag{II.19}$$

Note that the latter retains the linear reconstruction for u, and therefore it is second-order accurate for the advective term, but first-order accurate for the diffusive term. See discussions and results in Refs.[10, 11].

II.B.4. Boundary Conditions

Both strong and weak boundary conditions are considered. The residuals are defined at boundary nodes as

$$\mathbf{Res}_0 = -\mathbf{P}_0\left(\frac{\Phi_{1/2} - \Phi_0}{\Delta x_0} + \mathbf{s}_0\right), \tag{II.20}$$

$$\mathbf{Res}_N = -\mathbf{P}_N\left(\frac{\Phi_N - \Phi_{N-1/2}}{\Delta x_N} + \mathbf{s}_N\right), \tag{II.21}$$

where the dual volumes are define by $\Delta x_0 = (x_1 - x_0)/2$, $\Delta x_N = (x_N - x_{N-1})/2$. The weak boundary condition is implemented through the boundary numerical fluxes, $\Phi_0(\mathbf{u}_b, \mathbf{u}_0)$ and $\Phi_N(\mathbf{u}_N, \mathbf{u}_b)$, where $\mathbf{u}_b$ denotes a boundary state, which incorporates boundary conditions. For the Dirichlet problem considered here, the boundary state is defined as

$$\mathbf{u}_b = \begin{bmatrix} u_b \\ p_j \end{bmatrix}, \tag{II.22}$$

where $(u_b, p_j) = (2u(0) - u_0, p_0)$ for Φ_0, and $(u_b, p_j) = (2u(1) - u_N, p_N)$ for Φ_N. The value of u_b has been defined such that the average of u_j and u_b gives the boundary value: $(u_b + u_0)/2 = u(0)$ at $x = 0$ and $(u_b + u_N)/2 = u(1)$ at $x = 1$. The gradient variable in the boundary state is set by the numerical value stored at the boundary node since no boundary condition is given for p in the Dirichlet problem. These boundary residuals are solved together with the interior residuals. For more details, see discussions in Ref.[19], where a similar weak boundary condition procedure is discussed for a third-order cell-centered-type hyperbolic scheme.

In the strong boundary condition, we first compute the residuals at boundary nodes as described in the above. Then, we replace the first component of the residual, $\mathbf{Res}_j(1)$, by the following algebraic equation at boundary nodes, $j = 0$ and $j = N$:

$$\mathbf{Res}_0(1) = u_0 - u(0), \quad \mathbf{Res}_N(1) = u_N - u(1). \tag{II.23}$$

The other components $\mathbf{Res}_0(2)$ and $\mathbf{Res}_N(2)$ are retained, and will be solved together with the interior residuals and the above algebraic equations.

It is important to note that the physical boundary condition must be the same for the steady advection-diffusion equation and the first-order hyperbolic advection-diffusion equation because they are equivalent. The number of variables increases by the auxiliary variable p, but a scalar equation with a second-derivative is turned into two equations with first derivatives. Therefore, both differential equations involve two arbitrary constants, which are to be determined by two boundary conditions (see Appendix A). The hyperbolic formulation provides convenience when the boundary condition is given for the derivative, e.g., Neumann problems; the auxiliary variable can be directly specified without discretizing the solution derivative at a boundary. For example, a typical adiabatic condition at a viscous wall can be imposed in this way, i.e., zero normal heat flux via heat flux variables, just like an inviscid slip-wall condition for the velocity, in the hyperbolic Navier-Stokes schemes [3, 4, 7].

II.C. Target Solver

Our target solver is an implicit defect-correction solver:

$$\mathbf{U}^{k+1} = \mathbf{U}^k + \Delta\mathbf{U}, \tag{II.24}$$

where $\mathbf{U}$ is a global vector of numerical solutions, and the correction $\Delta\mathbf{U}$ is defined as the solution to the linearized system:

$$\mathbf{J}\Delta\mathbf{U} = -\mathbf{Res}(\mathbf{U}^k), \quad \mathbf{J} = \frac{\partial \mathbf{Res}^{(1)}}{\partial \mathbf{U}}. \tag{II.25}$$

Here, $\mathbf{Res}$ is a global residual vector for the target spatial discretization, and $\mathbf{Res}^{(1)}$ is a global vector of the first-order version of the target scheme, which is obtained by ignoring all LSQ gradients. Note that the first-order version of Scheme-II retains the linear reconstruction for u in Equation (II.19). Therefore, the contributions from the gradient terms in the linear reconstruction are included in the Jacobian $\mathbf{J}$ for Scheme-II. The linear system may be directly inverted or relaxed by a relaxation scheme. In this study, we relax the system by the sequential or multi-color Gauss-Seidel relaxation scheme to take advantage of the reduced numerical stiffness by the hyperbolic method.

III. Issues and Resolutions

Previous studies have demonstrated that both Scheme-I and Scheme-II experience no issues for high-Reynolds-number problems if the advective term dominates and the diffusive term is negligibly small [7, 10, 11]. However, issues arise in cases where $\nu \to 0$ but the advective and diffusive terms balance each other, e.g., inside a boundary layer. It has been reported [8, 9] that iterative solvers may diverge for high-Reynolds-number flows with boundary layers, but reducing the length scale L_r can resolve the issue. We have found also that even if the solver converges, the numerical solution can be catastrophically inaccurate for boundary layer problems with a strong dependence on the value of L_r.

In this section, we examine these problems in terms of L_r for a linear hyperbolic advection-diffusion system with $f^a = au$ and positive constants, a and ν:

$$\mathbf{f} = \mathbf{f}^a + \mathbf{f}^d = \begin{bmatrix} au \\ 0 \end{bmatrix} + \begin{bmatrix} -p \\ -u \end{bmatrix} = \begin{bmatrix} au - p \\ -u \end{bmatrix} = \begin{bmatrix} a & -1 \\ -1 & 0 \end{bmatrix} \mathbf{u}. \tag{III.1}$$

In the analyses that follow, the following parameters will play key roles:

$$Re = \frac{a}{\nu}, \quad Re_{L_r} = \frac{aL_r}{\nu}, \quad Re_{L_d} = \frac{aL_d}{\nu}, \quad Re_h = \frac{ah}{\nu}, \tag{III.2}$$

where Re is the Reynolds (or Peclet) number per grid unit length, Re_{L_r} is the relaxation Reynolds number, Re_{L_d} is the Reynolds number based on the diffusion length scale L_d, and Re_h is the mesh Reynolds number defined with a mesh spacing h.

III.A. Inaccuracy of Hyperbolic Schemes in Boundary Layers

The linear advection-diffusion equation with the boundary conditions $u(0) = 0$ and $u(1) = U_\infty = 1$ has the exact solution given by

$$u(x) = \frac{1 - \exp(Re_x)}{1 - \exp(Re)}, \quad Re_x = xRe, \tag{III.3}$$

which develops a boundary layer near at $x = 1$ for large Re. Numerical solutions are considered on a uniform grid with spacing h. Accuracy of numerical solutions is examined by the classical modal analysis [12, 14, 15]. Assume that the numerical solution is given in the form:

$$\mathbf{u}_j = \mathbf{U}c^j, \tag{III.4}$$

where $\mathbf{U} = (U, P)$ is a vector of amplitudes and c is a mode to be determined. Let us begin with the first-order version of Scheme-I. Substituting the modal solution (III.4) into the residual (II.9), we obtain

$$\mathbf{MU} = 0, \tag{III.5}$$

where

$$\mathbf{M} = \frac{1}{2hc}\begin{bmatrix} -a_v c^2 + 2(a + a_v)c - (a_v + 2a) & 1 - c^2 \\ \dfrac{-\nu c^2 + \nu}{T_r} & \dfrac{2hc}{T_r} - a_v(c-1)^2 \end{bmatrix}. \tag{III.6}$$

Non-trivial solutions exist if

$$\det(\mathbf{M}) = 0, \tag{III.7}$$

which can be factored as

$$(c-1)\left[\left(Re_{Lr}^2 + 2Re_{Lr} + Re_h\right)c^2 - \left(2Re_{Lr}^2 + 2Re_{Lr}Re_h + 2Re_{Lr} + Re_h\right)c + Re_{Lr}^2\right] = 0, \tag{III.8}$$

leading to three solutions:

$$c_1 = 1, \tag{III.9}$$

$$c_2 = \frac{2Re_{Lr}^2 + 2Re_{Lr}Re_h + 2Re_{Lr} + Re_h + \sqrt{(Re_h + 2Re_{Lr})\left(4Re_{Lr}^2Re_h + 4Re_{Lr}Re_h + 2Re_{Lr} + Re_h\right)}}{2(Re_{Lr}^2 + 2Re_{Lr} + Re_h)}, \tag{III.10}$$

$$c_3 = \frac{2Re_{Lr}^2 + 2Re_{Lr}Re_h + 2Re_{Lr} + Re_h - \sqrt{(Re_h + 2Re_{Lr})\left(4Re_{Lr}^2Re_h + 4Re_{Lr}Re_h + 2Re_{Lr} + Re_h\right)}}{2(Re_{Lr}^2 + 2Re_{Lr} + Re_h)}. \tag{III.11}$$

Expanding the mode c_3 for small h, we obtain

$$c_3 = \frac{Re_{Lr}}{Re_{Lr} + 2} + O(h), \tag{III.12}$$

which will be damped out with increasing j towards $x = 1$ for a finite Re_{L_r}. On the other hand, the mode c_2 can be expanded as

$$c_2^j = c_2^{\frac{x}{h}} = \exp(Re_x)\left(1 - \frac{Re_{Lr}^2 + Re_{Lr} + 1}{2Re_{Lr}}Re_xRe_h + O(h^2)\right). \tag{III.13}$$

This mode, together with c_1, approximates the exact solution (III.3) with first-order accuracy. These results indicate that accuracy of the numerical solution would be greatly affected by the relaxation Reynolds number Re_{Lr}. If $Re_{Lr} \to \infty$, then the mode c_3 will be hardly damped, and also the first-order error coefficient, $\frac{Re_{Lr}^2 + Re_{Lr} + 1}{2Re_{Lr}}$, will be unboundedly large. In fact, this is exactly the case with $L_r = L_d$: $Re_{Lr} \to \infty$ as $Re \to \infty$. To avoid these problems, we seek Re_{Lr} that minimizes the first-order error coefficient (see Figure 1). By solving

$$\frac{\partial}{\partial Re_{Lr}}\left(\frac{Re_{Lr}^2 + Re_{Lr} + 1}{2Re_{Lr}}\right) = 0, \tag{III.14}$$

for $Re_{Lr} > 0$, we obtain

$$Re_{Lr} = 1, \tag{III.15}$$

which gives

$$L_r = \frac{1}{Re}. \tag{III.16}$$

This formula confirms the observation reported in Refs.[8, 9] that the length scale needs to be reduced for high-Reynolds-number boundary layer problems. Remarkably, it also shows how it should be reduced: L_r needs to be inversely proportional to Re. Equation (III.16) implies also that the diffusive wave speed, which represents the dissipation coefficient of the upwind diffusion flux (II.11), remains finite and equal to the advective speed for any Reynolds number:

$$a_v = \frac{\nu}{L_r} = \nu Re = a. \tag{III.17}$$

It may be argued that the inaccuracy problem with the diffusion length scale $L_r = L_d$ is due to a lack of dissipation in the boundary layer. The dissipation matrix corresponding to the hyperbolic diffusion term is given by

$$\begin{bmatrix} a_v & 0 \\ 0 & T_r a_v/\nu \end{bmatrix}. \tag{III.18}$$

This matrix will vanish with $L_r = L_d$ for infinitely large Reynolds number because $a_v \to 0$ for $Re \to \infty$. Note that the factor T_r/ν is to be canceled by $\mathbf{P}_j$ as in Equation (II.9). In conventional schemes, as mentioned earlier, a lack of damping in the central diffusion scheme can be compensated by the dissipation term from the upwind advection scheme. In the hyperbolic method, such will not work since it will have no effects on the second component, but the new length scale $L_r = 1/Re$ successfully retains the entire matrix for $Re \to \infty$.

The new formula $L_r = 1/Re$ is obviously not optimal in pure diffusion problems. In the case that the hyperbolic advection-diffusion scheme is intended for use in diffusion dominated problems also, the following hybridization may be employed:

$$L_r = \min\left(1, \frac{1}{Re_{L_d}}\right) L_d, \tag{III.19}$$

so that we have $L_r = L_d$ for $Re_{L_d} \leq 1$ and $L_r = 1/Re$ for $Re_{L_d} > 1$. The above functional form has been chosen such that it is applicable to different diffusion length scales, e.g., slightly different L_d's in Refs.[1, 2], and also the hybridization factor can be expressed conveniently in terms of the relevant Reynolds number only.

For the first-order version of Scheme-II, we obtain

$$c_1 = 1, \tag{III.20}$$

$$c_2 = \frac{2Re_{Lr} + 2 + Re_h + \sqrt{8Re_{Lr}Re_h + (Re_h + 2)^2}}{2(Re_h - Re_{Lr} + 2)}, \tag{III.21}$$

$$c_3 = \frac{2Re_{Lr} + 2 + Re_h - \sqrt{8Re_{Lr}Re_h + (Re_h + 2)^2}}{2(Re_h - Re_{Lr} + 2)}. \tag{III.22}$$

The second and third modes can be expanded as

$$c_3 = \frac{Re_{Lr}}{Re_{Lr} + 2} + O(h), \tag{III.23}$$

$$c_2^j = c_2^{\frac{x}{h}} = \exp(Re_x)\left(1 - \frac{1}{2}Re_{Lr}Re_xRe_h + O(h^2)\right). \tag{III.24}$$

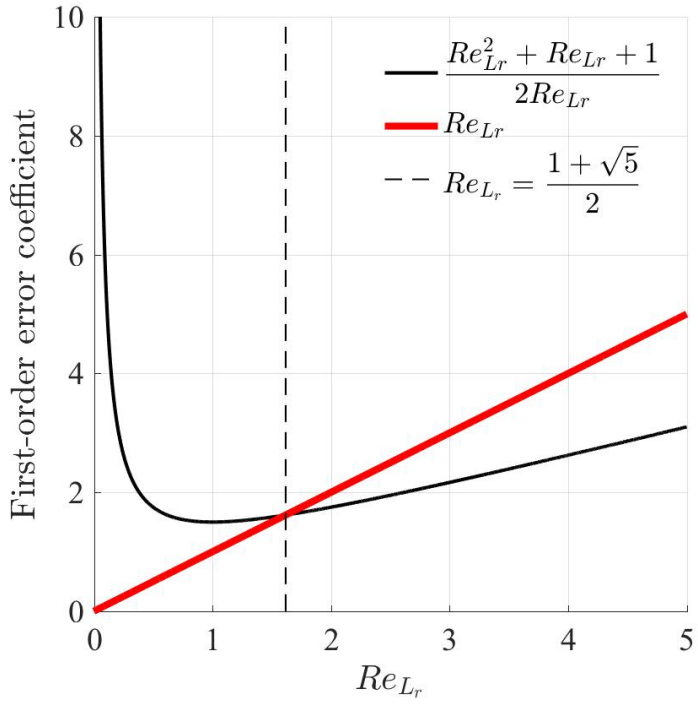

Figure 1: First-order error coefficients for Scheme-I, $\frac{(Re_{Lr}^2+Re_{Lr}+1)}{2Re_{Lr}}$, and for Scheme-II, Re_{Lr}. The crossing point is given by $Re_{Lr} = \frac{1+\sqrt{5}}{2}$, which is the so-called golden ratio, as indicated by the dashed line.

As before, a large numerical error is expected for $Re_{Lr} \to \infty$. But in this case, there is no positive value of Re_{Lr} that minimizes the first-order error. As shown in Figure 1, the error term coefficient is lower than that of Scheme-I for $Re_{Lr} < \frac{1+\sqrt{5}}{2}$, which includes $Re_{Lr} = 1$. In terms of the error magnitude, the optimal value of Re_{Lr} would be zero (i.e., $L_r = 0$), which eliminates the first-order error. However, vanishingly small Re_{Lr} will lead to an impractical scheme as we will discuss later.

An important conclusion drawn from the above analysis is that the relaxation length scale L_r needs to be defined as inversely proportional to Re, so that Re_{L_r} remains $O(1)$, and the dissipation of the upwind diffusion scheme is retained to combat high-frequency errors for high-Reynolds-number boundary-layer problems.

Remark: The length scale $L_r = 1/Re$ has been derived based on the first-order version of Scheme-I, and therefore it is not necessarily optimal for the second-order version of Scheme-I. The modal analysis for the second-order version is quite complicated, but the characteristic equation $\det(\mathbf{M}) = 0$ can be simplified by using one-sided finite-difference formulas for the gradients at the neighbor nodes to minimize the stencil size:

$$(c-1)\left[K_3 c^3 + K_2 c^2 - K_1 c + K_0\right] = 0, \tag{III.25}$$

where

$$K_3 = Re_{Lr}\left(Re_{Lr}+3\right)c^3, \quad K_2 = Re_{Lr}^2 + (7 - 4Re_h)Re_{Lr} + 4Re_h, \tag{III.26}$$

$$K_1 = 5Re_{Lr}^2 + (12Re_h + 7)Re_{Lr} + 4Re_h, \quad K_0 = 3Re_{Lr}\left(Re_{Lr}-1\right). \tag{III.27}$$

Solutions of the cubic equation are, however, still too complicated to be useful. To gain insight into the effect of second-order accuracy, we attempt to minimize the number of potential negative roots (i.e., oscillatory modes). By Decarte's rule of signs, we find that the minimum number of negative roots can be achieved if $K_2 > 0$ and $K_0 > 0$. These conditions are satisfied by

$$Re_{Lr} = \max\left(1, 4Re_h - \frac{7}{2}\right), \tag{III.28}$$

where $4Re_h - 7/2$ is an approximation to the positive root of $K_2 = 0$, which implies

$$L_r = \frac{K}{Re}, \quad K = \max\left(1, 4Re_h - \frac{7}{2}\right). \tag{III.29}$$

This means that the length scale is increased by a factor of $4Re_h - 7/2$ for $Re_h > 8/7$ in the second order scheme, or equivalently the dissipation coefficient $a_v = \nu/L_r$ is reduced. In the rest of the paper, the factor will be referred to as the second-order correction for Scheme-I. Numerical experiments show that the correction improves accuracy of the second-order scheme on under-resolved grids.

III.B. Convergence Deterioration

III.B.1. Analysis Method

In this section, we investigate effects of the new length scale $L_r = 1/Re$ on iterative convergence of the implicit solver. For simplicity, the second-order correction (III.29) is ignored here, and also the sequential GS linear relaxation scheme is considered. The sequential GS linear relaxation scheme and the implicit iteration scheme will be analyzed separately by a local Fourier analysis on a uniform grid of spacing h. To analyze the linear relaxation scheme, we insert a Fourier mode $\Delta\mathbf{U}_0 \exp(i\beta x/h)$, where $\Delta\mathbf{U}_0 = [\Delta u_0, \Delta p_0]$ is the amplitude and β is a frequency (or a phase change per h), into the sequential GS relaxation scheme,

$$\mathbf{J}_{ii}\Delta\mathbf{U}_i^{m+1} = \sum_{j=i-2}^{i-1} \mathbf{J}_{ij}\Delta\mathbf{U}_i^{m+1} + \sum_{j=i+1}^{i+2} \mathbf{J}_{ij}\Delta\mathbf{U}_i^{m}, \tag{III.30}$$

where $\mathbf{J}_{ii}$ is a 2×2 diagonal block of the Jacobian matrix at a node j, and $\mathbf{J}_{ij}$ is a 2×2 off-diagonal blocks for the neighbor j, and obtain

$$\Delta\mathbf{U}_0^{m+1} = \mathbf{G}\Delta\mathbf{U}_0^{m}, \tag{III.31}$$

where $\mathbf{G}$ is an amplification matrix. For stability, the spectral radius of $\mathbf{G}$, denoted by $\rho(\mathbf{G})$, must be less than 1. On the other hand, to analyze the implicit iteration scheme, we insert a Fourier mode $\mathbf{U}_0 \exp(i\beta x/h)$, where $\mathbf{U}_0 = [u_0, p_0]$, into the implicit solver with the linear system inverted, we obtain

$$\mathbf{U}_0^{k+1} = \left(\mathbf{I} - \mathbf{J}^{-1}\mathbf{R}\right)\mathbf{U}_0^{k}, \tag{III.32}$$

where $\mathbf{I}$ is the 2×2 identity matrix, $\mathbf{J}^{-1}$ is the inverse of the Fourier operator of the first-order Jacobian, and $\mathbf{R}$ is the second-order residual operator. The spectral radius of the operator, $\rho\left(\mathbf{I} - \mathbf{J}^{-1}\mathbf{R}\right)$, should be less than 1 for stability.

In both the linear relaxation and implicit iteration schemes, the spectral radius is computed numerically in the region of high Reynolds numbers: $(Re_h, Re) \in [10^{-3}, 10^{8}] \times [10^{3}, 10^{8}]$, excluding the region of $h > 1$. In both cases, slow convergence is indicated by the spectral radius smaller than but close to 1. Note that the analysis focuses on error damping, and does not take into account error propagation nor boundary condition effects. However, it provides useful indications of the performance of the relaxation and the implicit schemes. It should be noted also that the analysis is not specific to boundary layer problems, and therefore it is relevant to advection dominated problems with or without boundary layers. For this reason, we consider also the choice $L_r = L_d$ although our primary focus is on $L_r = 1/Re$.

III.B.2. Scheme-I

The spectral radius of the GS relaxation scheme is plotted in Figures 2(a) and 2(b) for $L_r = L_d$ and $L_r = 1/Re$, respectively. Note that no contours are shown in the region $h > 1$ (no grid points in the domain), and the red line is drawn along the line corresponding to $h = 10^{-3}$ (1001 grid points). For both relaxation length scales, the spectral radius is smaller than 1, and convergence is expected in the linear relaxation for high-Reynolds numbers. Figures 3(a) and 3(b) show the spectral radius contours of the implicit iteration for $L_r = L_d$ and $L_r = 1/Re$, respectively. A region of slow convergence is seen for high-Reynolds-numbers on refined grids for $L_r = L_d$, and it is completely removed by $L_r = 1/Re$. The analysis indicates that the formula $L_r = 1/Re$ not only minimizes the discretization error, but also improves the iterative convergence of Scheme-I for high-Reynolds-number problems.

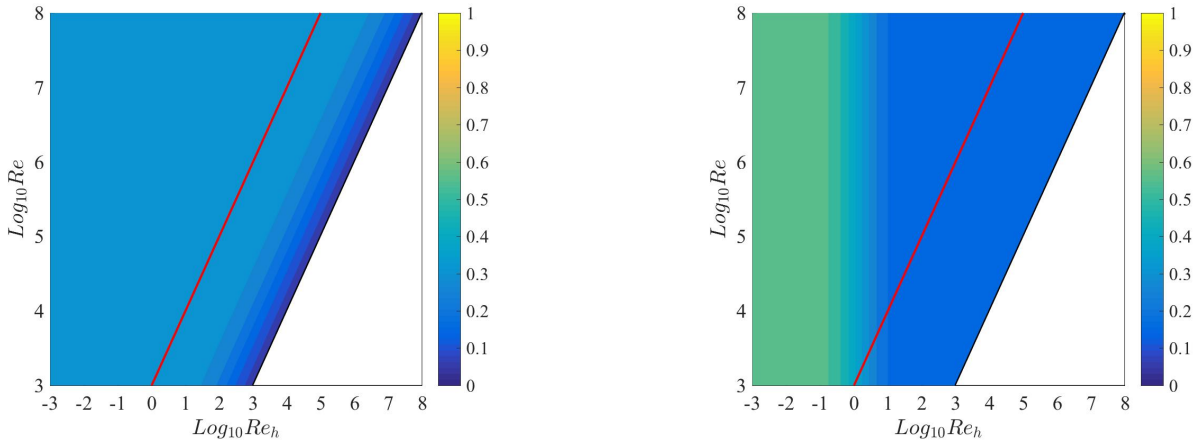

(a) $L_r = L_d$. (b) $L_r = 1/Re$.

Figure 2: Spectral radius of the GS relaxation scheme $\rho(\mathbf{G})$ for Scheme-I.

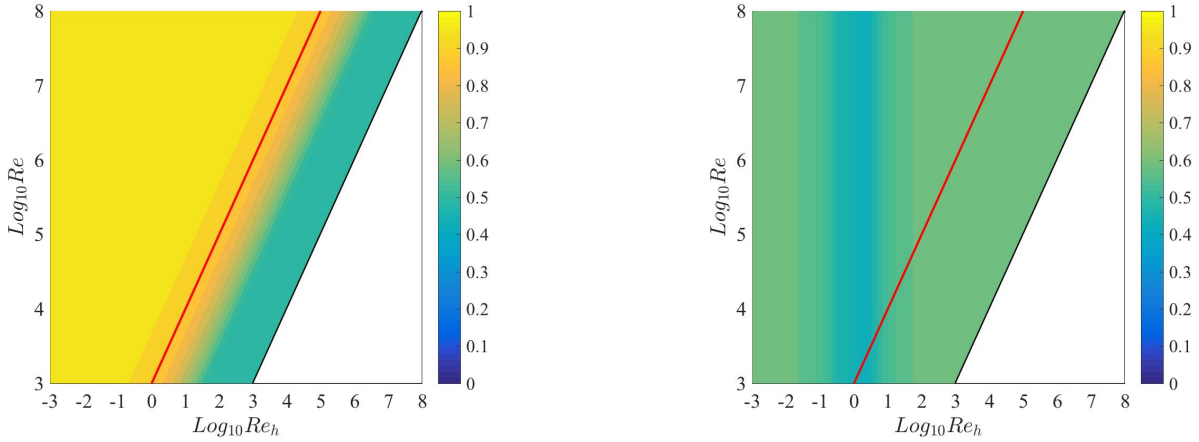

(a) $L_r = L_d$. (b) $L_r = 1/Re$.

Figure 3: Spectral radius of the implicit iteration scheme $\rho\left(\mathbf{I} - \mathbf{J}^{-1}\mathbf{R}\right)$ for Scheme-I.

III.B.3. Scheme-II

Scheme-II has issues in both linear relaxations and implicit iterations even with $L_r = 1/Re$. Figures 4(a) and 4(b) show the spectral radius contours for $L_r = L_d$ and $L_r = 1/Re$, respectively. As can be seen, the linear relaxation would converge with $L_r = L_d$, but suffer from extremely slow convergence with $L_r = 1/Re$ for high Re_h grids. However, for $L_r = L_d$, the implicit solver would experience convergence difficulties, as indicated in Figure 5(a), for highly refined grids, which is relevant, for example, to highly stretched boundary layer grids. For $L_r = 1/Re$, the implicit iteration converges rapidly as shown in Figure 5(b). Note, however, that the analysis for the implicit iteration assumes that the linear system is fully solved. Therefore, in reality, the implicit solver is not expected to converge because the linear relaxation would experience convergence problems (see Figure 4(b)). One might consider, then, applying the residual Jacobian based on Scheme-I instead, which has been shown to converge (see Figure 2(b)). Unfortunately, this strategy would not work. Figure 5(c), where Scheme-I Jacobian is denoted by $\mathbf{J}_I$, shows the spectral radius of the implicit iteration for Scheme-II with the Jacobian of Scheme-I. It shows that slow convergence occurs now in the implicit iteration. Yet another strategy would be to use the residual Jacobian based on Scheme-I as a preconditioner matrix in Jacobian-Free Newton-Krylov solvers. However, numerical experiments indicate that although it can prevent divergence, the solver can still be very slow to converge or stalls. These convergence problems appear to stem from a unique construction of Scheme-II and closely related to the mesh Reynolds number, which we discuss in the next section.

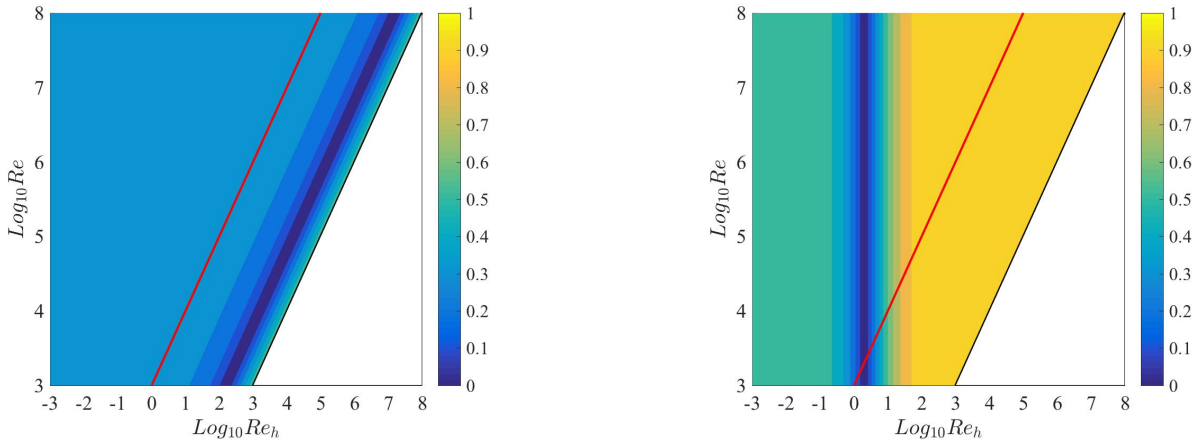

(a) $\rho(\mathbf{G})$ with $L_r = L_d$. (b) $\rho(\mathbf{G})$ with $L_r = 1/Re$.

Figure 4: Spectral radius of the GS relaxation scheme $\rho(\mathbf{G})$ for Scheme-II.

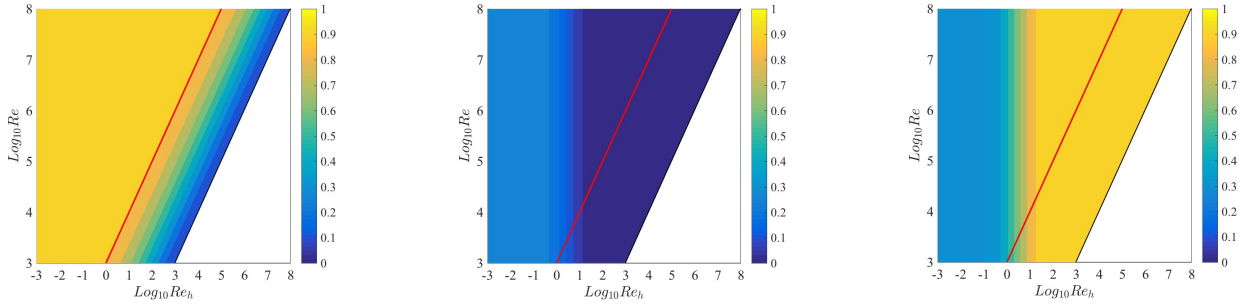

(a) $\rho\left(\mathbf{I}-\mathbf{J}^{-1}\mathbf{R}\right)$ with $L_r = L_d$. (b) $\rho\left(\mathbf{I}-\mathbf{J}^{-1}\mathbf{R}\right)$ with $L_r = 1/Re$. (c) $\rho\left(\mathbf{I}-\mathbf{J}_I^{-1}\mathbf{R}\right)$ with $L_r = 1/Re$.

Figure 5: Spectral radius of the implicit iteration scheme $\rho\left(\mathbf{I}-\mathbf{J}^{-1}\mathbf{R}\right)$ for Scheme-II.

III.C. Mesh-Reynolds-Number Restriction for Scheme-II

A close look at the numerical flux reveals potential issues with Scheme-II. To illustrate the issues, we begin with the first-order version of Scheme-I. Substituting the left and right states as in Equation (II.18) into the numerical flux (II.10), we obtain

$$\Phi(\mathbf{u}_L, \mathbf{u}_R) = \begin{bmatrix} a & -1 \\ -1 & 0 \end{bmatrix} \overline{\mathbf{u}} - \frac{1}{2} \begin{bmatrix} a + \dfrac{\nu}{Lr} & 0 \\ 0 & \dfrac{Lr}{\nu} \end{bmatrix} \Delta\mathbf{u}, \tag{III.33}$$

where $\overline{\mathbf{u}} = (\mathbf{u}_j + \mathbf{u}_{j+1})/2$ and $\Delta\mathbf{u} = \mathbf{u}_{j+1} - \mathbf{u}_j$. The first term on the right hand side is the consistent term, i.e., the term consistently approximating the physical flux (III.1). The second term is the dissipation term characterized by the positive definite dissipation matrix, which is required for an energy stability [10]. Now consider the first-order version of Scheme-II defined by the left and right states as in Equation (II.19), which results in

$$\Phi(\mathbf{u}_L, \mathbf{u}_R) = \begin{bmatrix} a & -\left\{1 - \dfrac{1}{2}\left(Re_h + \dfrac{h}{Lr}\right)\right\} \\ -1 & 0 \end{bmatrix} \overline{\mathbf{u}} - \frac{1}{2} \begin{bmatrix} a + \dfrac{\nu}{L_r} & \dfrac{Re_h}{2} \\ 0 & \dfrac{Lr}{\nu} - \dfrac{h}{2\nu} \end{bmatrix} \Delta\mathbf{u}. \tag{III.34}$$

Observe that the gradient terms in the linear reconstruction for u_L and u_R have generated additional contributions in both the consistent and dissipation terms. Two potential problems arise. First, the diffusion coefficient in the

consistent term has been altered:

$$1 - \frac{1}{2}\left(Re_h + \frac{h}{Lr}\right), \tag{III.35}$$

and it can be negative. Second, the altered dissipation matrix

$$\begin{bmatrix} a + \dfrac{\nu}{Lr} & \dfrac{Re_h}{2} \\ 0 & \dfrac{Lr}{\nu} - \dfrac{h}{2\nu} \end{bmatrix}, \tag{III.36}$$

may no longer be positive definite. These problems can lead to serious issues in the balanced high-Reynolds-number limit: $a\partial_x u = \partial_x p \neq 0$. On the other hand, issues would not be expected in the pure advection limit where $p = O(1/Re)$.

As one might expect, these problems are governed by the mesh Reynolds number. It is easy to show that the diffusion coefficient will be positive if

$$Re_h < \frac{2}{1 + 1/Re_{Lr}}, \tag{III.37}$$

and the dissipation matrix will be positive definite if

$$Re_h < 4\left[-(1 + 1/Re_{Lr}) + \sqrt{(1 + 1/Re_{Lr})\,(Re_{Lr} + 1 + 1/Re_{Lr})}\right]. \tag{III.38}$$

It can be shown that the former guarantees the latter:

$$Re_h < \frac{2}{1 + 1/Re_{Lr}} < 4\left[-(1 + 1/Re_{Lr}) + \sqrt{(1 + 1/Re_{Lr})\,(Re_{Lr} + 1 + 1/Re_{Lr})}\right], \tag{III.39}$$

and therefore both conditions are satisfied if

$$Re_h < \frac{2}{1 + 1/Re_{Lr}}. \tag{III.40}$$

This implies a mesh Reynolds number restriction for Scheme-II. Note that it leads to $Re_h < 0$ as $Re_{L_r} \to 0$. This is the reason that we cannot take arbitrarily small values of Re_{L_r} (or equivalently L_r) as mentioned in Section III.A. For the diffusion length scale $L_r = L_d$, we have $Re_{L_r} \to \infty$ for high-Reynolds-numbers, and the condition approaches the classical condition $Re_h < 2$, which is well known for the second-order central-difference scheme for the linear advection-diffusion equation [12, 14, 15]. However, it should be noted that the nature of the condition is quite different: the violation leads to a negative diffusion coefficient and a non-positive definite dissipation matrix in Scheme-II while it does not alter the diffusion coefficient nor the positiveness of the dissipation but merely generates numerical oscillations in the classical scheme. For $L_r = 1/Re$, the mesh Reynolds number restriction becomes

$$Re_h < 1. \tag{III.41}$$

In actual computations, however, serious problems (e.g., divergence in iterations) occur at much higher Re_h. Scheme-II can still be used for reasonably fine grids. However, it can easily diverge on irregular stretched grids that are typical in adapted unstructured grids for boundary layers. Two approaches are considered to overcome the problem.

(1)Improved Scheme-I: One possible approach is to follow Ref.[4] and improve Scheme-I so as to achieve third-order accuracy in the advective term. That is, we construct a higher-order LSQ gradient by evaluating a quadratic term with the LSQ gradient of the gradient variable, $(\partial_x p)_j$:

$$(\partial_x u)_j = \frac{\displaystyle\sum_{k\in\{k_j\}} \left(\mathbf{u}_k - \mathbf{u}_j - \frac{1}{2\nu}(\partial_x p)_j (x_k - x_j)^2\right)(x_k - x_j)}{\displaystyle\sum_{k\in\{k_j\}} (x_k - x_j)^2}, \tag{III.42}$$

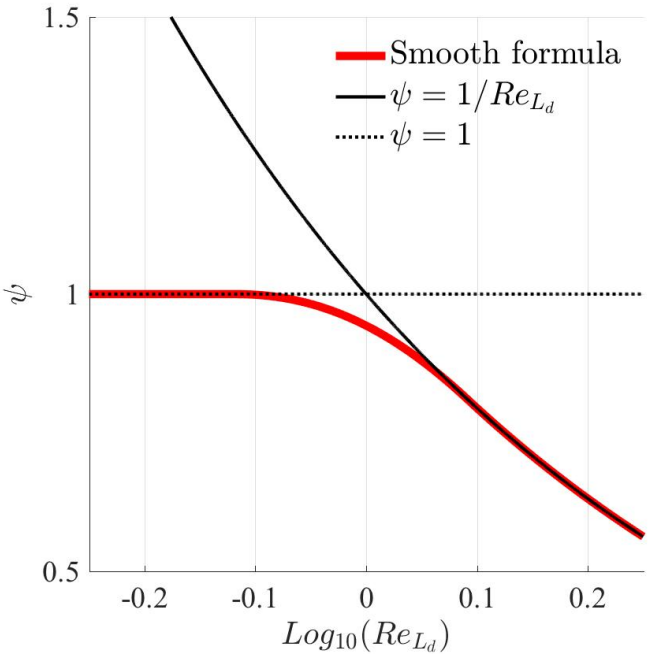

Figure 6: Smooth switching function ψ in Equation (IV.11).

which allows us to compute quadratic LSQ gradients within a compact linear-LSQ stencil. In this way, the scheme achieves third-order accuracy in the advective term without extending the stencil, which is the major attractive feature of Scheme-II. The mesh-Reynolds-number restriction (III.40) does not apply to the improved scheme because the solution gradients used in the linear reconstruction are not directly evaluated by the gradient variables. The improved scheme is called Scheme-IQ, and has been demonstrated for three-dimensional HNS schemes [4]. In all numerical experiments presented in this paper, we will focus on Scheme-IQ.

(2)Weak boundary condition: The other potential resolution is to employ a weak boundary condition at a solid wall in the boundary layer as widely employed in cell-centered schemes. It can be used also in the node-centered scheme considered here as described in Section II.B.4. On under-resolved grid where Re_h is large, the weak boundary condition is known to result in a numerical solution resembling a pure inviscid slip-wall solution [21, 22]. In effect, the weak boundary condition will turn a high-Reynolds-number boundary-layer flow into, where there is no sufficient resolution, a nearly inviscid flow, for which the hyperbolic schemes are known to work successfully [11]. In fact, the weak boundary condition approach works very well for Scheme-II, at least in one dimension, as will be numerically demonstrated later.

IV. Extension to Viscous Burgers Equation

Consider the viscous Burgers equation, which is given by Equation (II.1) with $f^a = u^2/2$:

$$u\partial_x u = \nu \partial_{xx} u. \tag{IV.1}$$

This equation has a boundary-layer-type solution with $u = 0$ at $x = 0$, and $u = -1$ at $x = 1$:

$$u(x) = -\tanh\left(\frac{x}{2\nu}\right), \tag{IV.2}$$

which exhibits a boundary layer near $x = 0$ for small ν. Equation (IV.1) can be thought of as a nondimensionalized equation with the x-coordinate scaled by the domain size L, and u by U_∞, which is the magnitude of the solution at $x = 1$. Then, the diffusion coefficient ν is equivalent to the reciprocal of the 'free stream' Reynolds number, $Re_\infty = U_\infty L/\nu_\infty$:

$$\nu = \frac{1}{Re_\infty}, \tag{IV.3}$$

where ν_∞ is the constant diffusion coefficient in the dimensional viscous Burgers equation, and the exact solution is expressed as

$$u(x) = -\tanh\left(\frac{xRe_\infty}{2}\right). \tag{IV.4}$$

We solve this problem by the hyperbolic viscous Burgers system:

$$\partial_\tau u + u\partial_x u = \partial_x p, \quad \partial_\tau p = \frac{\nu}{T_r}\left(\partial_x u - \frac{p}{\nu}\right), \tag{IV.5}$$

where $T_r = L_r^2/\nu$. As in the linear case, we have found numerically that the diffusion relaxation length scale $L_r = L_d$ causes troubles in both accuracy and iterative convergence for a boundary layer. To resolve the issues, we extend the improved definition (III.16) as

$$L_r = \frac{1}{Re}, \quad Re = \frac{|u|}{\nu}, \tag{IV.6}$$

so that the diffusive wave speed remains finite and equal to the local advective speed,

$$a_v = \frac{\nu}{L_r} = |u|. \tag{IV.7}$$

It is important to note that the local advective speed $|u|$ on the above equations is defined by Equation (II.13) and therefore will never vanish. However, Re can still become vanishingly small for a very large diffusion coefficient. To take into consideration such diffusion dominated cases, we consider the following formula:

$$L_r = \psi(Re_{L_d})L_d, \quad Re_{L_d} = \frac{|u|L_d}{\nu}, \tag{IV.8}$$

where $\psi(Re_{L_d})$ denotes a switching function that is 1 for small Re_{L_d} and $1/Re_{L_d}$ for large Re_{L_d}. The formula considered in the linear case, i.e., Equation (III.19), corresponds to

$$\psi(Re_{L_d}) = \min\left(1, \frac{1}{Re_{L_d}}\right), \tag{IV.9}$$

or

$$\psi(Re_{L_d}) = \min\left(1, \frac{K}{Re_{L_d}}\right), \tag{IV.10}$$

for Scheme-I, where K is the second-order correction defined by Equation (III.29), where Re_h is evaluated by the local solution value. The relaxation length scale L_r in the numerical flux is evaluated by the averaged reconstructed solution at the interface, i.e., $(u_L + u_R)/2$, and L_r in the matrix $\mathbf{P}_j$ is evaluated by the values at the node j. By numerical experiments, we have found that a free stream evaluation of ψ, i.e., with $Re_{L_d} = \frac{U_\infty L_d}{\nu}$ equally works well. The numerical results are so similar that no significant differences were observed from those obtained by the local formula described above.

Remark: In the nonlinear case, a smooth function may be desired to avoid potential convergence difficulties due to the non-differentiability of the formula at $Re_{L_d} = 1$. One possible smooth formula, in the case of no second-order correction, is

$$\psi(Re_{L_d}) = \begin{cases} 1 & \text{for } Re_{L_d} < 1-\delta, \\ 1/Re_{L_d} & \text{for } Re_{L_d} > 1+\delta, \\ \dfrac{Re_{L_d}(21+5\delta)(Re_{L_d}^2 - Re_{L_d} + 10\delta + 2)}{32} & \text{otherwise,} \end{cases} \tag{IV.11}$$

where $\delta = \sqrt{5} - 2$. See Figure 6. For problems considered in this paper, however, no significant differences are observed for the smooth and non-smooth functions.

V. Extension to Hyperbolic Navier-Stokes System

We consider the hyperbolic Navier-Stokes system introduced in Ref.[7], which has been extended to three dimensions in Ref.[3]. This system, called HNS20, consists of the compressible Navier-Stokes equations and fifteen extra equations for the density and velocity gradients, and the heat fluxes. The HNS20 system has three relaxation-time parameters [3,7]:

$$T_\rho = \frac{L_\rho^2}{\nu_\rho}, \quad T_v = \frac{L_v^2}{\nu_v}, \quad T_h = \frac{L_h^2}{\nu_h}, \tag{V.1}$$

$$\nu_\rho = V_{min}, \quad \nu_v = \frac{4\mu}{3\rho}, \quad \nu_h = \frac{\gamma\mu}{Pr}, \tag{V.2}$$

where V_{min} is the minimum dual control volume for a given grid, ρ is the density, μ is the viscosity defined by Sutherland's law, γ is the ratio of specific heats, Pr is the Prandtl number, L_ρ, L_v, and L_h are length scales associated with the density gradient, the velocity gradients, and the heat fluxes. In the previous studies [3,4,5,6,7], these length scales are unified and defined by a single formula, but here we define them separately. By extending the formula (IV.8), we define

$$L_\rho = \psi(Re^\rho_{L_d})L_d, \qquad Re^\rho_{L_d} = \frac{|u|L_d}{\nu_\rho}, \tag{V.3}$$

$$L_v = \psi(Re^v_{L_d})L_d, \qquad Re^v_{L_d} = \frac{|u|L_d}{\nu_v}, \tag{V.4}$$

$$L_h = \psi(Re^h_{L_d})L_d, \qquad Re^h_{L_d} = \frac{|u|L_d}{\nu_h}, \tag{V.5}$$

where $|u|$ is the local flow speed. The switching function ψ is given by Equation (IV.10) for Scheme-I/IQ, and by Equation (IV.9) otherwise. The limiting procedure (II.13) with $\delta = 0.01$ is applied to $|u|$ in the above formulas; therefore $|u|$ will never vanish. As in the viscous Burgers case, a free stream evaluation of ψ, i.e., with U_∞ instead of $|u|$ and the free stream values of ν_v and ν_h, has been found to work equally well as will be shown later. The free stream version is very useful as it makes L_r a global constant and simplifies the implementation.

In the previous study [4], a combination of $L_\rho = L_h = L_d$ and the following formula has been found to resolve issues effectively:

$$L_v = \frac{L_r^{\text{JCP2010}}}{1/2 + \sqrt{Re_{L_r^{\text{JCP2010}}} + 1/4}}, \quad Re_{L_r^{\text{JCP2010}}} = \frac{\rho_\infty U_\infty L_r^{\text{JCP2010}}}{\mu_\infty}, \tag{V.6}$$

where L_r^{JCP2010} denotes the length scale in Ref.[2] (see Equation (B.6) in Appendix B). In this study, we have found that the following simpler version, applied to all length scales, also works very well:

$$L_v = \frac{L_d}{\sqrt{Re^{v_\infty}_{L_d}}}, \qquad Re^{v_\infty}_{L_d} = \frac{U_\infty L_d}{\nu_{v\infty}}, \tag{V.7}$$

$$L_\rho = \frac{L_d}{\sqrt{Re^{\rho_\infty}_{L_d}}}, \qquad Re^{\rho_\infty}_{L_d} = \frac{U_\infty L_d}{\nu_\rho}, \tag{V.8}$$

$$L_h = \frac{L_d}{\sqrt{Re^{h_\infty}_{L_d}}}, \qquad Re^{h_\infty}_{L_d} = \frac{U_\infty L_d}{\nu_{h\infty}}, \tag{V.9}$$

where $\nu_{v\infty}$ and $\nu_{h\infty}$ are the free stream values of ν_v and ν_h, respectively. Numerical experiments show that these formulas provide practical approximations to the formulas in Equations (V.3)-(V.5), and also to their free-stream versions. The success of these formulas (V.6) and (V.7)-(V.9) seems to lie in the slightly reduced dissipation caused by the square root, which has a similar effect as the second-order correction in ψ.

VI. Numerical Results

For model equations, schemes to be tested are listed in Table 1. Scheme-IQ(L_d) and Scheme-II(L_d) are based on the diffusion length scale $L_r = L_d$. Scheme-IQ(ψ) and Scheme-II(ψ) are based on the improved length scale

Scheme	Discretization					Diffusive Jacobian
	Advection		Diffusion			
	Flux	LSQ (u)	Flux	LSQ (p)	L_r	
Alpha	Upwind	Linear	Alpha	None	N/A	Damping-only
Galerkin	Upwind	Linear	Galerkin	None	N/A	Exact
Scheme-IQ(L_d)	Upwind(3rd)	C-quadratic	Upwind	Linear	L_d	Scheme-I(1st)
Scheme-IQ(ψ)	Upwind(3rd)	C-quadratic	Upwind	Linear	ψL_d	Scheme-I(1st)
Scheme-II(L_d)	Upwind(3rd)	None	Upwind	Linear	L_d	Scheme-II(1st)
Scheme-II(ψ)	Upwind(3rd)	None	Upwind	Linear	ψL_d	Scheme-II(1st)
Scheme-II(ψ)-JacI	Upwind(3rd)	None	Upwind	Linear	ψL_d	Scheme-I(1st)
Scheme-II(JCP2010)	Upwind(3rd)	None	Upwind	Linear	L_r^{JCP2010}	Scheme-II(1st)

Table 1: Summary of discretizations and Jacobians. Advective Jacobian is the exact derivative of the first-order upwind scheme for all. Order of accuracy is indicated by 2nd and 3rd in the parentheses. Scheme-II(JCP2010) an upwind flux constructed by the eigen-structure of the hyperbolic advection-diffusion system (see Appendix C), and the length scale L_r as described in Ref.[2].

$L_r = \psi L_d$, where the switching function ψ is given by Equation (IV.9) for the linear advection-diffusion equation, and by Equation (IV.11) for the viscous Burgers equation. The second-order correction (III.29) is applied to Scheme-IQ for all problems: $\psi = K/Re_{L_d}$ is used whenever $\psi = 1/Re_{L_d}$ in Equation (IV.11).

For comparison, conventional schemes are also tested for two-dimensional model problems. Both schemes use the same second-order upwind scheme as the hyperbolic schemes, but differ by the diffusion scheme. The scheme using the alpha-damping diffusion scheme with $\alpha = 1$ [20, 16] is referred to as Alpha, and the other using the Galerkin diffusion scheme, which is implemented in the edge-based form, is referred to as Galerkin. These conventional schemes are implemented with the strong boundary condition. Details for the Navier-Stokes schemes will be given later.

VI.A. One-Dimensional Problems

In one dimension, we consider boundary-layer problems for the linear advection-diffusion equation and the viscous Burgers equation. In both cases, stretched irregular grids are generated by the mapping

$$x_i = \frac{1 - \exp(\alpha \xi_i)}{1 - \exp(\alpha)}, \tag{VI.1}$$

where $\xi_0 = 0$, $\xi_N = 1$, and $\xi_i = \frac{i + 0.45(r - 0.5)}{N}$, $i = 1, 2, 3, \ldots, N-1$, N is the number of nodes, r is a random number in $[0, 1]$, and $\alpha = 18.0$ for all cases. Three levels of grids are considered with $N = 33$, 65, and 128. These grids are referred to as Grid1, Grid2, and Grid3, respectively. The mesh Reynolds number, which varies in space due to non-uniform spacings, is computed for the three grids, and plotted in Figure 7. The coarsest grid is under-resolved with $Re_h > 2$ for almost all cels, and the finest grid may be considered as fully resolved with $Re_h < 2$ inside the boundary layer. The edge of the boundary layer is indicated by the dashed line, which is determined by the exact solution for the linear advection-diffusion equation.

For all problems, the initial solution for u is set by the exact solution with random perturbations. The gradient variable p is initialized by the LSQ gradient of the perturbed initial solution u. The iterative solver is taken to be converged when the maximum of the L_1 residual norm is reduced by ten orders of magnitude. All convergence histories will be given by the maximum of the residual norms scaled by the corresponding initial residual norms over all equations. For all cases, error convergence results will be presented, unless otherwise stated, for relative errors: the L_1 norm of the difference between numerical solutions and exact solutions at nodes divided by the maximum of the exact solution in the entire domain.

VI.A.1. Linear Advection Diffusion Equation with Strong Boundary Condition

We consider the boundary layer problem for the linear advection-diffusion equation as described in Section III.A with the exact solution given by Equation (III.3). To demonstrate the applicability of the improved algorithm for a negative value of a, we take $a = -1$ and $\nu = |a|/Re$, where $Re = 10^8$. Boundary conditions are $u(0) = 0$ and $u(1) = 1$, which are imposed strongly at boundary nodes as described in Section II.B.4. Here, we compare Scheme-IQ(L_d), Scheme-IQ(ψ), Scheme-II(ψ), Scheme-II(ψ)-JacI, Scheme-II(JCP2010).

Iterative convergence results are shown in Figure 8. As expected from the analysis in Section III.B, Scheme-IQ(L_d) does not converge on all grids; it eventually blows up. Scheme-II(ψ) diverges on the coarsest grid for which $Re_h > 1$, but it converges on finer grids although only by two orders of magnitude. The use of the Jacobian based on Scheme-I helps Scheme-II(ψ) converge on the coarsest grid, and converge further down on the finer grids (six and eight orders of magnitude reduction for the medium and finest grids, respectively), but it takes thousands of iterations to converge. On the other hand, Scheme-IQ(ψ) converged on all grids, demonstrating the effectiveness of the new length scale. Also, Scheme-II(JCP2010) converges on all grids although it experiences some difficulty on Grid1. The results indicate that Scheme-II can be made convergent by constructing the dissipation matrix based on the eigen-structure of the unified hyperbolic advection-diffusion system. Figure 9 shows the number of linear relaxations at each iteration. As expected, Scheme-II(ψ) has a problem in the linear relaxation; it cannot reduce the linear residual by one order even with 1000 relaxations (which is set as the maximum) in many cases. The linear relaxation improves with the Jacobian based on Scheme-I, but it does not improve the implicit iteration convergence very much as predicted by the analysis in Section III.B and confirmed numerically as shown in Figure 8.

Figure 10 shows error convergence results for the schemes that converged on all grids: Scheme-IQ(ψ), Scheme-II(ψ)-JacI, and Scheme-II(JCP2010). The results show that Scheme-IQ(ψ) and Scheme-II(JCP2010) yield second-order accuracy in the solution variable u as well as in the gradient $\partial_x u = p/\nu$. However, Scheme-II(ψ)-JacI gives larger errors in u as shown in the figure, and too large errors for the coarsest grid to fit in the figure although the errors in the gradient are reasonably small for the two fine grids. Solution and gradient are plotted in Figure 11. It is observed that Scheme-IQ(ψ) and Scheme-II(JCP2010) capture the boundary layer accurately. For Scheme-II(ψ)-JacI, the solution is very inaccurate on the coarsest grid, but looks reasonably accurate for the finer grids. These results indicate that just improving the iterative convergence of Scheme-II is not a very meaningful strategy.

VI.A.2. Linear Advection Diffusion Equation with Weak Boundary Condition

We consider the same linear problem as in the previous section for the weak boundary conditions. The residuals are defined and the numerical solutions are computed at all nodes, including boundary nodes as described in Section III.C. Here, we consider the schemes Scheme-IQ(L_d), Scheme-IQ(ψ), and Scheme-II(ψ).

Figure 12 shows iterative convergence histories. First, it can be seen that Scheme-IQ(L_d) does not converge on all grids even with the weak boundary condition; it eventually blows up. On the other hand, Scheme-IQ(ψ) and Scheme-II(ψ) achieve ten orders of magnitude reduction in the residual on all grids. Figure 13 shows the number of linear relaxations. The linear relaxation now converges for Scheme-II although it takes more relaxations than other schemes. As discussed in Section III.C, these results confirm that Scheme-II can be made to work with the weak boundary condition.

Figure 14 shows the error convergence results. As expected, Scheme-IQ(ψ) and Scheme-II(ψ) yield second-order accuracy for both the solution and gradient. These schemes produce accurate solutions on all grids as can be seen in Figure 15; the latter gives more accurate solutions than the former as predicted for first-order schemes in Section III.A.

VI.A.3. Viscous Burgers Equation with Weak Boundary Condition

To demonstrate the improved algorithm for a nonlinear problem, we consider the problem described in Section IV for the viscous Burgers equation with $Re_\infty = 10^8$. For this problem, we consider Scheme-IQ(ψ) with the strong and weak boundary conditions, and Scheme-II(ψ) with the weak boundary condition. Figure 16 shows iterative convergence histories. All schemes successfully converged on all grids. As shown in Figure 17, the linear relaxation converges for all schemes. Second-order accuracy has been observed for both schemes as shown in Figure 18. These schemes accurately capture the boundary layer as can be observed in Figure 19. These results demonstrate that the improved algorithms perform well also for the nonlinear Burgers equation. The presented results have been obtained with L_r defined by Equation (IV.8) with ψ as in Equation (IV.10) for Scheme-IQ, and with ψ as in

Equation (IV.9) for Scheme-II, but results are very similar if L_r is evaluated by the free stream value, and therefore not shown.

VI.B. Two-Dimensional Problems

We consider the linear advection-diffusion problem in two dimensions:

$$a\partial_x u + b\partial_y u = \nu(\partial_{xx} u + \partial_{yy} u), \tag{VI.2}$$

where $(a, b) = (0.52, -0.86,)$ and ν is determined from a given Reynolds number Re,

$$Re = \frac{\sqrt{a^2 + b^2}}{\nu}. \tag{VI.3}$$

In all cases, we set $Re = 10^6$, and investigate the performance of the hyperbolic schemes. This equation has an exact solution in a unit square domain with boundary layers:

$$u(x, y) = \frac{[1 - \exp(a(x-1)/\nu)][1 - \exp(b(y-1)/\nu)]}{[1 - \exp(-a/\nu))][1 - \exp(-b/\nu)]}. \tag{VI.4}$$

The boundary layers are developed at $x = 1$ and $y = 0$ for large values of a/ν and b/ν, respectively. Here, we take a restricted domain with $x = 0.125$ and focus on the one at $y = 0$. Later, we also consider an advection dominated problem without boundary layers, and investigate the behaviors of the hyperbolic schemes with the improved length scale.

Computational grids are generated with quadrilateral and triangular elements. For the boundary layer problem, we consider regular but stretched quadrilateral grids, and stretched irregular triangular grids. These grids are referred to as Grid-SQ and Grid-ST. For the advection dominated problem, we employ irregular isotropic triangular grids, which is referred to as Grid-T. The coarsest levels of these grids are shown in Figure 20, with contours of exact solutions used.

Boundary conditions are imposed either strongly or weakly. For the weak condition, the residual is computed at a boundary node with the accuracy-preserving boundary quadrature formula derived in Ref.[23]. The fluxes at boundary nodes are computed by the same numerical flux used in the interior scheme with the right state specified by boundary conditions. In the Dirichlet condition considered here, the solution variable u and the gradient along the boundary are specified by the boundary condition, and the normal gradient is set by the current value at the node. In the strong boundary condition, the residuals are computed as above, and then replace two of the residual components by the algebraic equations for the solution and the tangential gradient. See Ref.[4, 23] for details.

Scheme-I(ψ) and Scheme-II(ψ) for the two-dimensional advection-diffusion equation are described in Ref.[11]. Scheme-IQ(ψ) uses the compact quadratic LSQ gradients for the solution variable u as described in Ref.[4]. For Scheme-IQ, the second-order correction (III.29) is applied with Re_h evaluated at a node by using the minimum height of elements sharing the node. For all problems, we attempt to reduce the residuals by ten orders of magnitude in the L_1 norm for all equations. The GS relaxation scheme is used to relax the linear system in the implicit solver to reduce the linear residual by one order of magnitude. Error convergence results will be presented for absolute errors: the L_1 norm of the difference between numerical solutions and exact solutions at nodes in the entire domain. As in one dimension, the pseudo time is dropped completely. Initial solutions are set by the exact solution with random perturbations.

VI.B.1. Regular Quadrilateral Grids.

Regular quadrilateral grids have been generated in the domain $(x, y) \in [0, 0.125] \times [0, 10^{-4}]$, with $n \times n$ nodes, where $n = 33$, 65, 129, and 257, which will be referred to as Grid-SQ1, Grid-SQ2, Grid-SQ3, and Grid-SQ4, respectively. The grids have uniform but different spacings in x and y directions with the cell aspect ratio 1250. Mesh Reynolds numbers, based on the uniform vertical cell spacing h_y, are $Re_h = Re \times h_y = 3.12$, 1.56, 0.781, 0.391. See Figure 20(a) for the coarsest grid and the exact solution contours. For this problem, only the strong boundary condition is considered. For a comparison purpose, the conventional scheme, Alpha, is also tested for this problem.

Figures 21, 22, and 23 show iterative convergence histories, the number of linear relaxations, and residual convergence versus CPU time, respectively. As expected from the one-dimensional analysis in Section III.B.2, Scheme-IQ(L_d) converges extremely slowly although the linear relaxation converges fast. We terminated the calculations for Scheme-IQ(L_d), and will not discuss its results any further below. On the other hand, Scheme-IQ(ψ)

and Scheme-II(ψ) converge rapidly as shown in Figures 21(a)-21(d). However, the linear relaxation slows down on coarse grids in the case of Scheme-II(ψ) as predicted in Section III.B.3. The conventional scheme converges rapidly, but the linear relaxation slows down significantly for fine grids due to the stiffness of the second-order diffusion term. As a result, the hyperbolic schemes converge faster in CPU time than the conventional scheme for the finest grid as shown in Figure 23(d).

Error convergence results are shown in Figures 24(a), 24(b), and 24(c) for u, $\partial_x u$, and $\partial_y u$, respectively. In the conventional scheme, the gradients are computed by a linear LSQ method. The results show that the hyperbolic schemes achieve second-order accuracy for all variables as expected. The conventional scheme also gives nearly second-order accuracy for all variables for this problem. Solutions and the normal gradients, which are relevant to the viscous stress in viscous simulations, along a vertical line at $x = 0.0625$ are plotted in Figures 25 and 26. As expected from the one-dimensional analysis, Scheme-II(ψ) gives slightly more accurate solution profile than Scheme-IQ(ψ). Observe also that the conventional scheme is less accurate than the hyperbolic schemes in the prediction of the gradient near the bottom boundary at $y = 0$.

The results confirm that Scheme-II(ψ) works, even with the strong boundary condition on regular quadrilateral grids, as long as Re_h is small enough. For irregular grids, however, Re_h is not clearly defined, and Scheme-II(ψ) fails even on highly refined grids as we discuss in the next section.

VI.B.2. Irregular Triangular Grids.

Highly-stretched irregular grids have been generated in the domain $(x, y) \in [0, 0.125] \times [0, 1.25 \times 10^{-5}]$, with $n \times n$ nodes, where $n = 33$, 65, and 129, which will be referred to as Grid-ST1, Grid-ST2, Grid-ST3, respectively. These grids have higher resolutions in the boundary layer than the quadrilateral grids in the previous section. The mesh Reynolds number, which is evaluated by the minimum height of elements sharing a node; it is less than 1 for all grids. The cell aspect ratio ranges from $O(10^3)$ to $O(10^5)$ based on the ratio of the longest side to the shortest height of triangular elements. For this problem, we consider Scheme-IQ(ψ) and Scheme-II(ψ) with both strong and weak boundary conditions, and also Scheme-II(JCP2010) with the strong condition. For comparison, the conventional scheme, Galerkin, is also tested for this problem.

Figures 27, 28, and 29 show iterative convergence, the number of linear relaxations, and residual convergence versus CPU time, respectively. Observe that Scheme-II(ψ) diverges on the two fine grids even with the weak boundary condition although it converges, surprisingly, on the coarsest grid. However, Scheme-II(JCP2010) converges on all grids although it exhibits slow down in a later stage of convergence. These results indicate that Scheme-II(ψ) is not robust, but can be made convergent by improving the dissipation matrix. On the other hand, Scheme-IQ(ψ) converges on all grids; it converges faster with the weak boundary condition than with the strong boundary condition. Scheme-IQ(L_d), again, exhibits extremely slow convergence. It is observed also that the conventional scheme slows down in the linear relaxation for fine grids. As a result, Scheme-IQ(ψ) converges faster in CPU time for fine grids as shown in Figure 29.

Error convergence results are shown in Figure 30, where only the converged cases (on all grids) are shown. Both conventional and hyperbolic schemes achieve second-order accuracy in the solution variable u. The gradients obtained by the conventional scheme with a linear LSQ method are one-order lower as expected. The hyperbolic schemes achieves second-order accuracy in the gradient in the y direction (see Figure 30(c)), but yield first-order accuracy in the gradient in the direction perpendicular to the stretched direction (y) as shown in Figure 30(b). In particular, Scheme-II(JCP2010) gives significantly larger errors. The lower-order gradient accuracy in the direction of the larger spacing on anisotropic grids has not been reported before, and is a subject for future study.

Solution and gradient profiles along a vertical line at $x = 0.0625$ are shown Figures 31 and 32, respectively. As can be seen, Scheme-IQ(ψ) yields very accurate solutions and gradients. Also, it is observed that Scheme-II(ψ) gives very accurate solutions on the coarsest grid. As is well known, the hyperbolic scheme gives very smooth gradients whereas conventional schemes generate oscillations in the gradients on irregular grids, which can be observed in these results (even on the finest grid).

VI.B.3. Advection Dominated Problem without Boundary Layer.

To investigate effects of the improved length scale on advection dominated problems without a boundary layer, we consider a smooth problem in the unit square domain with the exact solution [24]:

$$u(x, y) = \cos(2\pi\eta) \exp\left(\frac{-8\pi^2\nu}{1 + \sqrt{1 + 16\pi^2\nu^2}}\,\xi\right), \tag{VI.5}$$

where $\xi = ax+by$, $\eta = bx-ay$. Computational grids are irregular isotropic triangular grids with $n \times n$ nodes, where $n = 17$, 33, and 65. See Figure 20(c) for the coarsest grid and the exact solution contours. This problem does not involve boundary layers, and therefore it is essentially a pure advection problem. In this limit, the second-order hyperbolic schemes are known to achieve third-order accuracy in the solution variable u as mentioned in Section II.B. Here, the strong boundary condition is used. Scheme-I(L_d), Scheme-I(ψ), Scheme-II(L_d) and Scheme-II(ψ) are tested, and compared with the conventional scheme with the Galerkin diffusion disctetization.

Figures 33, 34, and 35, show iterative convergence, the number of linear relaxations, and residual versus CPU time, respectively. First, we see that Scheme-IQ(ψ) converges faster than Scheme-IQ(L_d) for finer grids. The better performance of Scheme-IQ(ψ) may be due to the added dissipation by the new length scale; Scheme-IQ(L_d) loses the dissipation of the upwind diffusion flux for high Reynolds numbers and keeps only the dissipation from the upwind advection scheme. Second, for Scheme-II, it can be seen that Scheme-II(L_d) converges on all grids, which is expected from the results in Ref.[11]. However, Scheme-II(ψ) diverges on all grids. This is consistent with the analysis in Section III.B.3. Scheme-II(ψ) with the Scheme-I Jacobian allows the linear relaxation converges, but the implicit iteration now does not converge, which is also consistent with the analysis. In comparison with the conventional scheme, it is seen that hyperbolic schemes are not faster in CPU time than the conventional scheme, which is expected since diffusion is negligibly small in this problem, but the additional cost may be justified in that Scheme-IQ(ψ) is a third-order scheme for this problem as discussed below.

Figure 36 shows the error convergence results. Third-order accuracy of the hyperbolic schemes can be observed in Figure 36(a). For the gradients, first-order accuracy by the conventional scheme and second-order accuracy by the hyperbolic schemes are confirmed as shown in Figures 36(b) and 36(c). Note that Scheme-IQ(L_d) and Scheme-IQ(ψ) achieve nearly the same error levels for all variables. This is due to the second-order correction in the length scale, which effectively increases L_r and therefore reduces the dissipation. Without the correction, the error are actually slightly larger with Scheme-IQ(ψ) because of the twice as large dissipation.

VI.C. Compressible Navier-Stokes Results

Effects of the improved length scale formula have been studied for a laminar flow over a flat plate at $M_\infty = 0.5$ with $Pr = 0.72$ and $\gamma = 1.4$. The domain is taken to be rectangular $(x, y, z) \in [-2, 1] \times [0, 1] \times [0, 3]$, where the flat plate is located at the bottom ($z = 0$) and $(x, y) \in [0, 1] \times [0, 1]$. Four levels of tetrahedral grids are generated with a parabolic stretching applied across the boundary layer to provide a uniform boundary-layer resolution over the flat plate. These grids have 32, 64, 128, and 192 nodes over the flat plate, and approximately 12, 24, 48, 80 nodes inside the boundary layer, with the total number of nodes: 6048, 24384, 97920, and 220608. The coarsest grid is shown in Figure 37(a), and the solution contours are shown in Figure 37(b). A reference value of the drag coefficient is 0.001328 based on the Blasius solution of the incompressible flow over a flat plate [25]. A periodic boundary condition is used at boundary planes at $y = 0$ and $y = 1$, and a symmetry condition is applied at $z = 0$ ahead of the flat plate. The free stream condition is used at the inflow boundary ($x = -2$), and the back pressure condition is used at the top ($z = 3$) and outflow ($x = 1$) boundaries. Numerical experiments have been performed for $Re_\infty = 10^6$, where Re_∞ is the free stream Reynolds number based on the length in the x-direction of the flat plate. The mesh Reynolds number computed based on converged numerical solutions near the flat plate are $Re_h = 22$, 6.9, 2.3, and 1.1 for the four levels of grids.

The new length scales in Section V have been implemented in the HNS solver within NASA's FUN3D code [26], which is a well-validated 3D unstructured-grid solver developed by NASA Langley Research Center. For demonstration, we consider the HNS20-I scheme with various length scale options. The scheme with the length scales defined as in Equations (V.3)-(V.5) is referred to as HNS20-I(ψ), and the same scheme with the free stream evaluation of the length scales is referred to as HNS20-I(ψ_∞). To demonstrate the effect of the second-order correction, we also consider the one without the second-order correction, which is referred to as HNS20-I(ψ_0). Finally, HNS20-I($1/\sqrt{Re_\infty}$) refers to the scheme with the free stream approximations, Equations (V.7)-(V.9). These HNS schemes are compared with the default FUN3D scheme, which uses the same inviscid scheme but the Galerkin discretization for the viscous terms. In all schemes, a pseudo-time term is used with CFL=200, and linear system is relaxed by a multi-color Gauss-Seidel scheme with 15 relaxations per iteration. See Ref.[4] for details.

Figure 38(a) shows the iterative residual convergence for the continuity equation on the finest grid. FUN3D, HNS20-I(ψ), HNS20-I(ψ_∞), and HNS20-I($1/\sqrt{Re_\infty}$) show very similar convergence histories except that HNS20-I($1/\sqrt{Re_\infty}$) shows an irregular behavior near the end of the convergence. The irregular convergence is observed only on the finest grid. On the other hand, HNS20-I(ψ_0) takes more iterations to converge, indicating the impact of the second-order correction term and effectiveness of the free stream approximation for L_r. Similarly, the drag coefficient also converges in a similar manner for FUN3D, HNS20-I(ψ), HNS20-I(ψ_∞), and HNS20-I($1/\sqrt{Re_\infty}$), and slower convergence is observed for HNS20-I(ψ_0).

Figure 39(a) shows the drag coefficient convergence versus h_{eff}, which is the L_1 norm of the dual control volumes. All HNS 20 schemes except HNS20-I(ψ_0) give superior drag predictions than FUN3D, demonstrating the effectiveness of the new length scales and the free stream approximation, and the impact of the second-order correction. Figure 39(b) shows the drag coefficient convergence versus h_{DoF}, where h_{DoF} represents an effective mesh spacing based on the discrete problem size:

$$h_{DoF} = \frac{1}{\sqrt[3]{N_{eqs}N}}, \tag{VI.6}$$

where $N_{eqs} = 5$ for the FUN3D scheme and $N_{eqs} = 20$ for the HNS20 schemes, and N is the total number of nodes. It is observed that the HNS20 schemes, HNS20-I(ψ), HNS20-I(ψ_∞), and HNS20-I($1/\sqrt{Re_\infty}$), yield more accurate drag prediction for the same h_{DoF}, i.e., for the same number of discrete unknowns. This means that the HNS scheme can be faster in CPU time than the FUN3D scheme for the same level of accuracy in the drag prediction.

To demonstrate that the HNS20 schemes not only yield accurate drag predictions but also superior pointwise skin friction predictions, we compare the skin friction distributions obtained by HNS20-I(ψ), HNS20-I(ψ_∞), HNS20-I($1/\sqrt{Re_\infty}$), and FUN3D. As shown in Figure 40(a), the HNS schemes yield more accurate skin-friction distributions than FUN3D over the entire flat plate. In Figure 40(b), the skin friction is plotted against $log_{10}x$ to show the details near the leading edge. It can be seen that the HNS schemes yield more accurate skin friction further towards the leading edge, and that HNS20-I(ψ) and HNS20-I(ψ_∞) yield slightly more accurate distributions than HNS20-I($1/\sqrt{Re_\infty}$).

VII. Concluding Remarks

Issues encountered by the hyperbolic Navier-Stokes method for high-Reynolds-number boundary-layer problems have been discussed. Analyses have been performed for a one-dimensional advection-diffusion problem, and resolutions have been proposed. Extensive numerical experiments are presented to verify the proposed resolutions. A major finding is that the relaxation length scale must be defined to be inversely proportional to the Reynolds number to avoid problems in accuracy and iterative convergence, which has been derived by minimizing errors in the first-order version of Scheme-I. The improved length scale has been shown to provide additional dissipation to recover accuracy and cure convergence problems for high-Reynolds number boundary-layer flows. Scheme-IQ, which achieves higher-order in the inviscid approximation, has been demonstrated to provide robust and accurate hyperbolic schemes for practical viscous applications. Other findings are summarized as below:

1. The improved length scale greatly improves iterative convergence of Scheme-I and Scheme-IQ.

2. The improved length scale has been derived for the first-order version of Scheme-I, and a second-order correction should be applied to second-order versions of Scheme-I and Scheme-IQ on under-resolved grids.

3. For nonlinear problems, the length scale needs to be defined by local solution values, but the free stream evaluation still provides an effective approximation. In the Navier-Stokes case, $L_r \propto 1/\sqrt{Re_\infty}$ has also been found to give a good approximation, but a similar formula leads to inaccurate results for the viscous Burgers equation.

4. The improved length scale provides superior iterative convergence also for high-Reynolds-number problems without boundary layers (i.e., inviscid limit), and does not degrade accuracy for Scheme-I and Scheme-IQ. Hyperbolic schemes achieve third-order accuracy in the inviscid limit as designed.

5. Hyperbolic schemes converge faster in CPU time than conventional schemes as a grid is refined to better resolve a boundary layer.

6. Hyperbolic schemes constructed based on the eigen-structure of the hyperbolic advection-diffusion system do not experience issues for boundary-layer problems. It implies that the high-Reynolds-number issues may be resolved by directly modifying the dissipation matrix, instead of modifying the length scale.

7. Scheme-II introduces a negative diffusion coefficient and loses positive definiteness of the upwind dissipation matrix for large mesh-Reynolds-numbers, leading to accuracy and convergence problems for boundary-layer problems. A weak boundary condition has been found to resolve the issues, but not entirely successful. The improved length scale is required for boundary layers, but it leads to convergence problems for advection dominated problems without boundary layers; it needs to be switched back to the diffusion length scale. For Scheme-I, none of these issues apply.

8. It was observed that hyperbolic schemes lost accuracy of the derivative by one order in the direction of larger grid spacing for highly-stretched irregular triangular grids although the error level was much lower in comparison with a conventional scheme.

Future work should focus on the last two items to enable efficient and robust high-Reynolds-number simulations by Scheme-II, and to understand the cause of degraded gradient accuracy on highly-stretched irregular triangular grids.

Acknowledgments

This work has been funded by the U.S. Army Research Office under the contract/grant number W911NF-12-1-0154 with Dr. Matthew Munson as the program manager, and by NASA under Contract No. NNL09AA00A with Dr. Veer N. Vatsa as the technical monitor. The first author gratefully acknowledges support from Software CRADLE.

References

[1]Nishikawa, H., "A First-Order System Approach for Diffusion Equation. I: Second Order Residual Distribution Schemes," *J. Comput. Phys.*, Vol. 227, 2007, pp. 315–352.

[2]Nishikawa, H., "A First-Order System Approach for Diffusion Equation. II: Unification of Advection and Diffusion," *J. Comput. Phys.*, Vol. 229, 2010, pp. 3989–4016.

[3]Nakashima, Y., Watanabe, N., and Nishikawa, H., "Hyperbolic Navier-Stokes Solver for Three-Dimensional Flows," *54th AIAA Aerospace Sciences Meeting*, AIAA Paper 2016-1101, San Diego, CA, 2016.

[4]Liu, Y. and Nishikawa, H., "Third-Order Inviscid and Second-Order Hyperbolic Navier-Stokes Solvers for Three-Dimensional Inviscid and Viscous Flows," *46th AIAA Fluid Dynamics Conference*, AIAA Paper 2016-3969, Washington, D.C., 2016.

[5]Nishikawa, H., "New-Generation Hyperbolic Navier-Stokes Schemes: $O(1/h)$ Speed-Up and Accurate Viscous/Heat Fluxes," *Proc. of 20th AIAA Computational Fluid Dynamics Conference*, AIAA Paper 2011-3043, Honolulu, Hawaii, 2011.

[6]Nishikawa, H., "First, Second, and Third Order Finite-Volume Schemes for Navier-Stokes Equations," *Proc. of 7th AIAA Theoretical Fluid Mechanics Conference, AIAA Aviation and Aeronautics Forum and Exposition 2014*, AIAA Paper 2014-2091, Atlanta, GA, 2014.

[7]Nishikawa, H., "Alternative Formulations for First-, Second-, and Third-Order Hyperbolic Navier-Stokes Schemes," *Proc. of 22nd AIAA Computational Fluid Dynamics Conference*, AIAA Paper 2015-2451, Dallas, TX, 2015.

[8]Nakashima, Y., Private Communication, 2015.

[9]Baty, H. and Nishikawa, H., "Hyperbolic Method for Magnetic Reconnection Process in Steady State Magnetohydrodynamics," *Mon. Not. R. Astron. Soc.*, Vol. 459, 2016, pp. 624–637.

[10]Nishikawa, H., "First-, Second-, and Third-Order Finite-Volume Schemes for Diffusion," *J. Comput. Phys.*, Vol. 256, 2014, pp. 791–805.

[11]Nishikawa, H., "First, Second, and Third Order Finite-Volume Schemes for Advection-Diffusion," *J. Comput. Phys.*, Vol. 273, 2014, pp. 287–309.

[12]Shyy, W., "A Study of Finite Difference Approximations to Steady-State Convection-Dominated Flow Problems," *J. Comput. Phys.*, Vol. 57, 1985, pp. 415–438.

[13]Leonard, B. P., "Order of Accuracy of QUICK and Related Convection-Diffusion Schemes," *Appl. Math. Modell.*, Vol. 19, 1995, pp. 644–653.

[14]Hirsch, C., *Numerical Computation of Internal and External Flows*, Vol. 2, A Wiley - Interscience Publications, 1990.

[15]Wesseling, P., *Principles of Computational Fluid Dynamics*, Springer, 2000.

[16]Nishikawa, H., "Robust and Accurate Viscous Discretization via Upwind Scheme - I: Basic Principle," *Comput. Fluids*, Vol. 49, No. 1, October 2011, pp. 62–86.

[17]van Leer, B., Lee, W.-T., and Powell, K. G., "Sonic-Point Capturing," *Proc. of 9th AIAA Computational Fluid Dynamics Conference*, AIAA Paper 1989-1945, 1989.

[18]Katz, A. and Sankaran, V., "An Efficient Correction Method to Obtain a Formally Third-Order Accurate Flow Solver for Node-Centered Unstructured Grids," *J. Sci. Comput.*, Vol. 51, 2012, pp. 375–393.

[19]Nishikawa, H. and Roe, P. L., "Third-Order Active-Flux Scheme for Advection Diffusion: Hyperbolic Diffusion, Boundary Condition, and Newton Solver," *Computers and Fluids*, Vol. 125, 2016, pp. 71–81.

[20]Nishikawa, H., "Beyond Interface Gradient: A General Principle for Constructing Diffusion Schemes," *Proc. of 40th AIAA Fluid Dynamics Conference and Exhibit*, AIAA Paper 2010-5093, Chicago, 2010.

[21]Bazilevs, Y. and Hughes, T. J. R., "Weak Imposition of Dirichlet Boundary Conditions in Fluid Mechanics," *Computers and Fluids*, Vol. 36, 2007, pp. 12–26.

[22]Abbas, Q. and Nordstrom, J., "Weak versus Strong No-Slip Boundary Conditions for The Navier-Stokes Equations," *Eng. Appl. Comp. Fluid.*, Vol. 4, No. 1, 2010, pp. 29–38.

[23]Nishikawa, H., "Accuracy-Preserving Boundary Flux Quadrature for Finite-Volume Discretization on Unstructured Grids," *J. Comput. Phys.*, Vol. 281, 2015, pp. 518–555.

[24]Nishikawa, H. and Roe, P. L., "On High-Order Fluctuation-Splitting Schemes for Navier-Stokes Equations," *Computational Fluid Dynamics 2004*, edited by C. Groth and D. W. Zingg, Springer-Verlag, 2004, pp. 799–804.

[25]White, F. M., *Viscous Fluid Flow*, McGraw-Hill, 2nd ed., 1991.

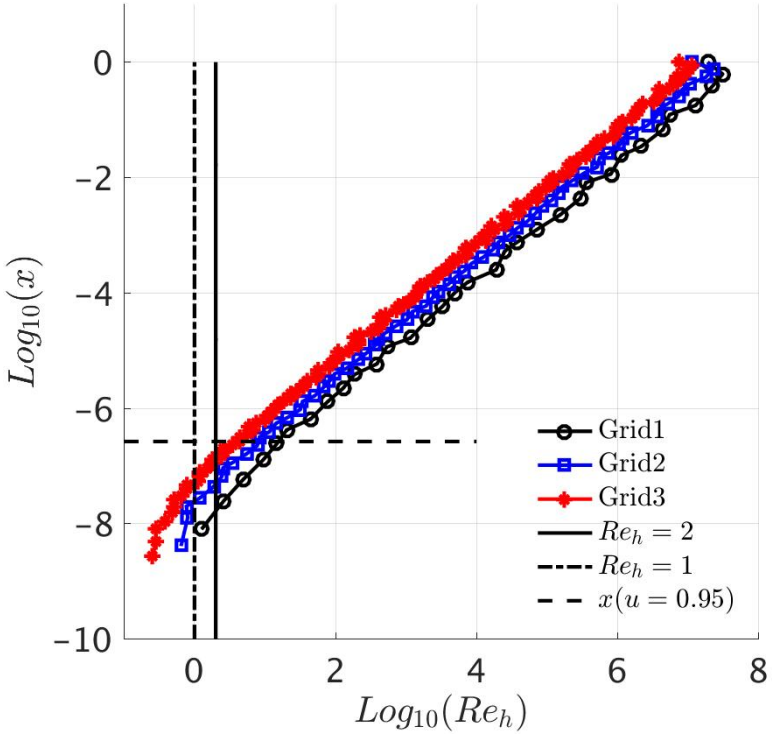

Figure 7: Mesh Reynolds number distributions.

[26]Biedron, R. T., Carlson, J.-R., Derlaga, J. M., Gnoffo, P. A., Hammond, D. P., Jones, W. T., Kleb, B., Lee-Rausch, E. M., Nielsen, E. J., Park, M. A., Rumsey, C. L., Thomas, J. L., and Wood, W. A., "FUN3D Manual: 12.9," *NASA-TM–2016–219012*, February 2016.

[27]Toro, E. F. and Montecinos, G. I., "Advection-diffusion-reaction equations: Hyperbolisation and high-order ADER discretizations," *SIAM J. Sci. Comput.*, Vol. 36, 2014, pp. A2423–A2457.

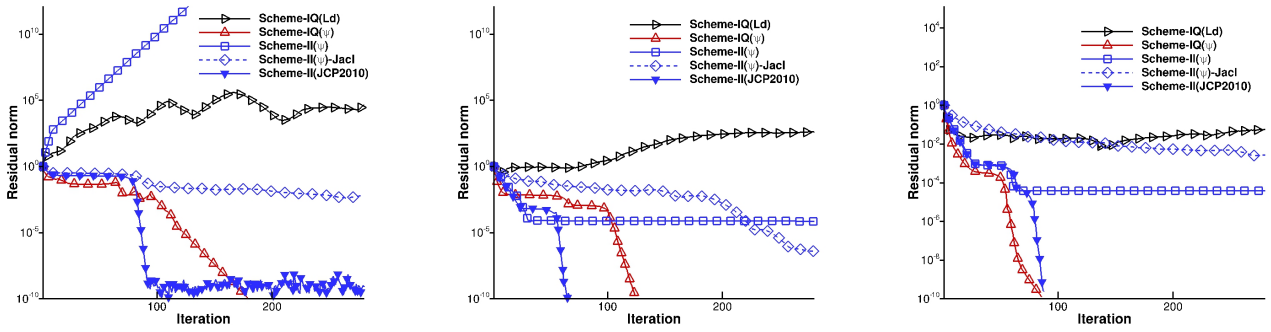

(a) Grid1: 32 nodes. (b) Grid2: 64 nodes. (c) Grid3: 128 nodes.

Figure 8: Iterative convergence results for the linear problem with strong boundary conditions.

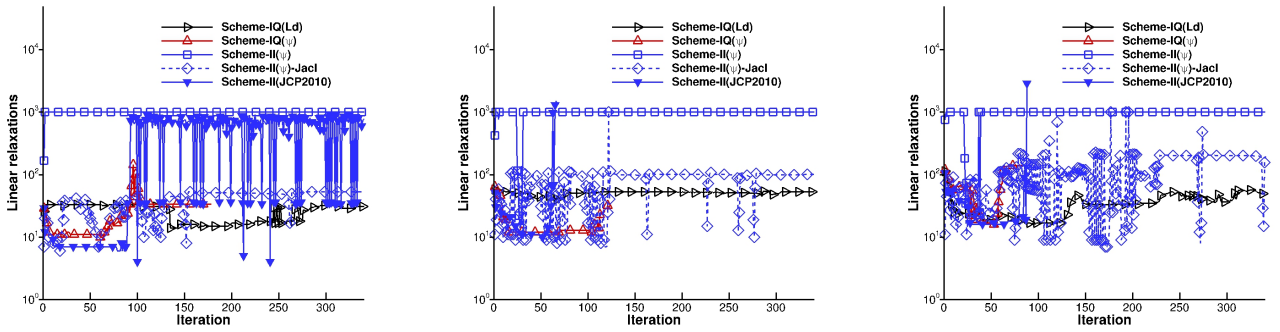

(a) Grid1: 32 nodes. (b) Grid2: 64 nodes. (c) Grid3: 128 nodes.

Figure 9: GS relaxations for the linear problem with strong boundary conditions.

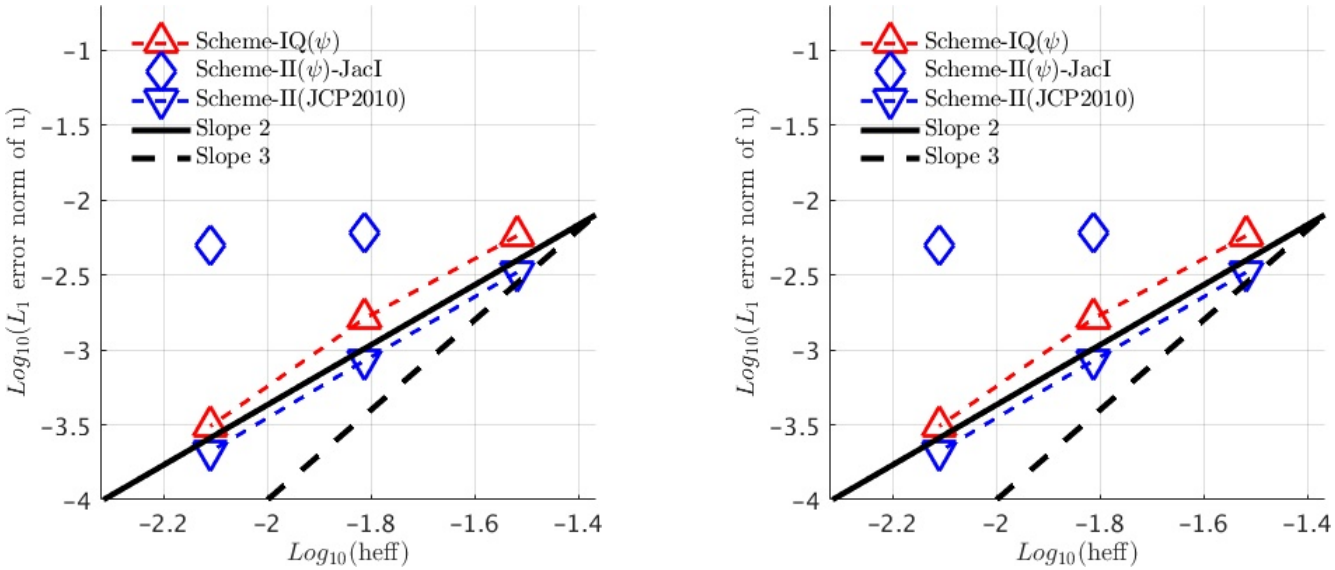

(a) Solution. (b) Gradient.

Figure 10: Error convergence results for the linear problem with strong boundary conditions.

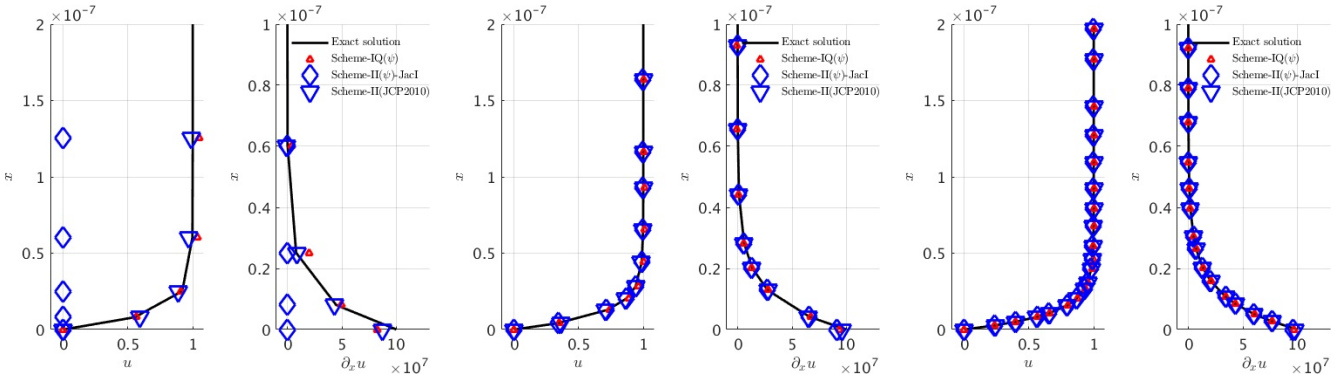

(a) Grid1: 32 nodes. (b) Grid2: 64 nodes. (c) Grid3: 128 nodes.

Figure 11: Solutions and gradients for the linear problem with strong boundary conditions.

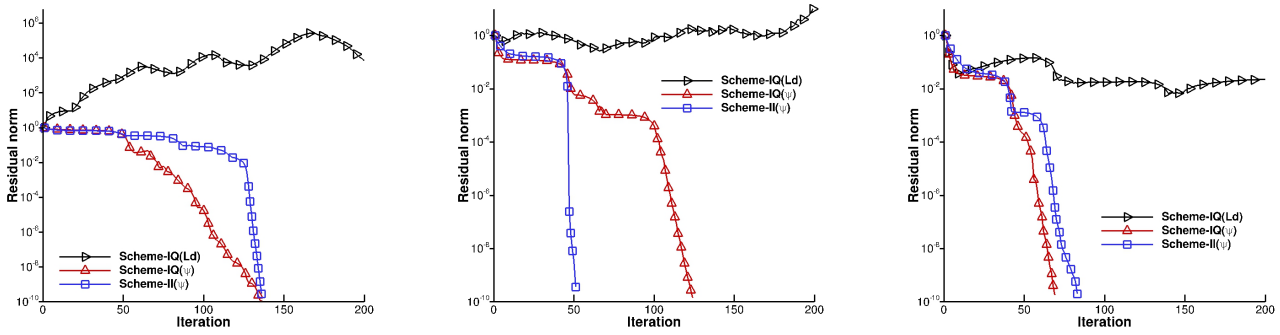

(a) Grid1: 32 nodes. (b) Grid2: 32 nodes. (c) Grid3: 128 nodes.

Figure 12: Iterative convergence results for the linear problem with weak boundary conditions.

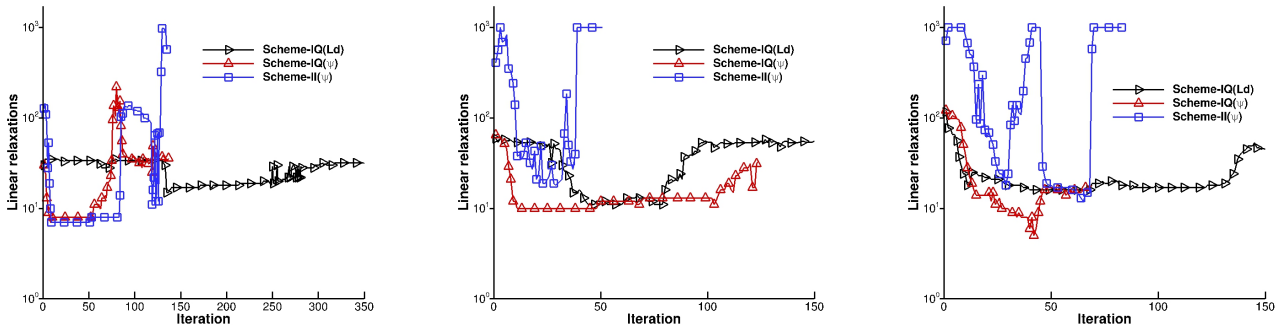

(a) Grid1: 32 nodes. (b) Grid2: 32 nodes. (c) Grid3: 128 nodes.

Figure 13: GS relaxations for the linear problem with weak boundary conditions.

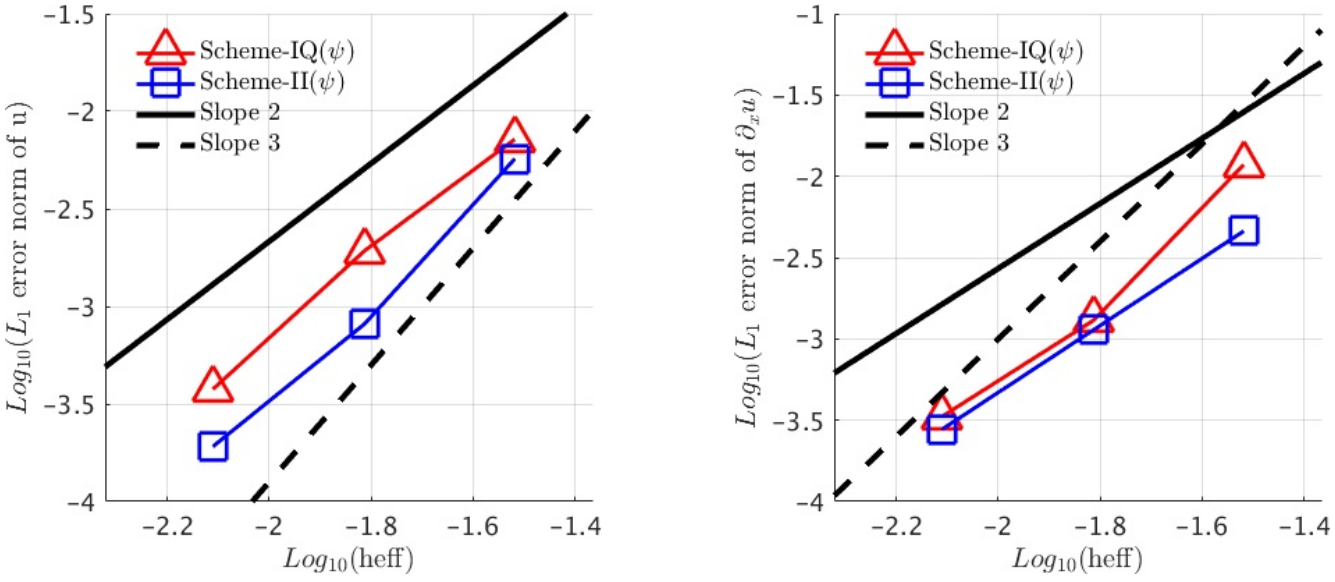

(a) Solution. (b) Gradient.

Figure 14: Error convergence results for the linear problem with weak boundary conditions.

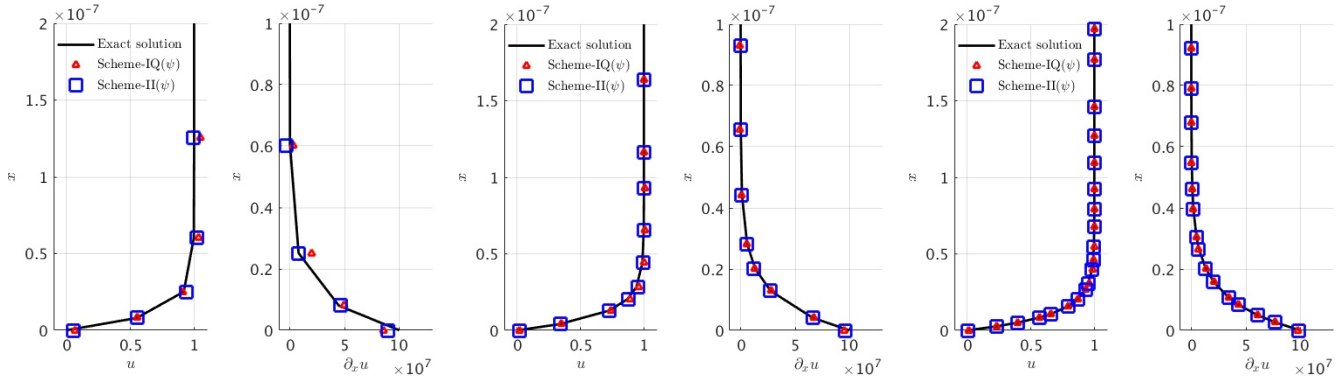

(a) Grid1: 32 nodes. (b) Grid2: 64 nodes. (c) Grid3: 128 nodes.

Figure 15: Solutions and gradients for the linear problem with weak boundary conditions.

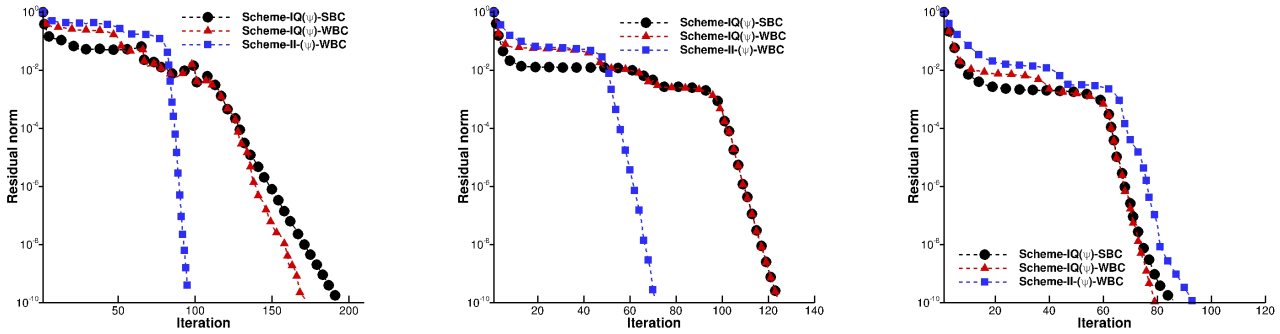

(a) Grid1: 32 nodes. (b) Grid2: 64 nodes. (c) Grid3: 128 nodes.

Figure 16: Iterative convergence results for the nonlinear problem.

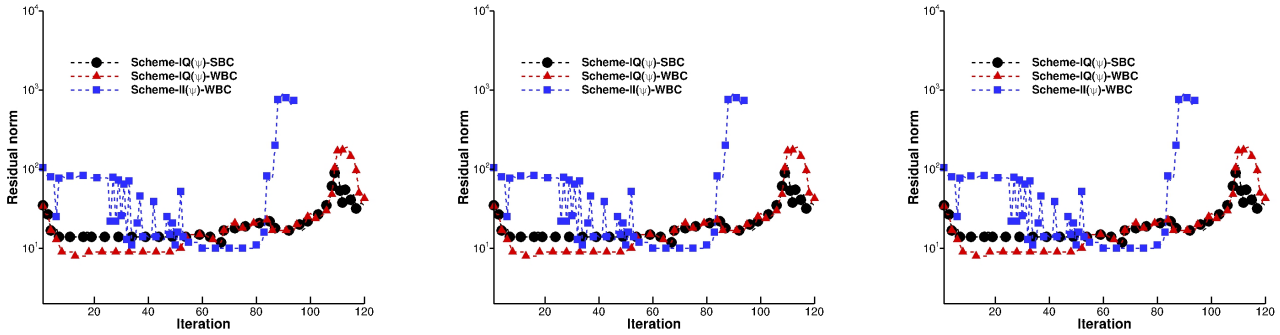

(a) Grid1: 32 nodes. (b) Grid2: 64 nodes. (c) Grid3: 128 nodes.

Figure 17: GS relaxations for the nonlinear problem.

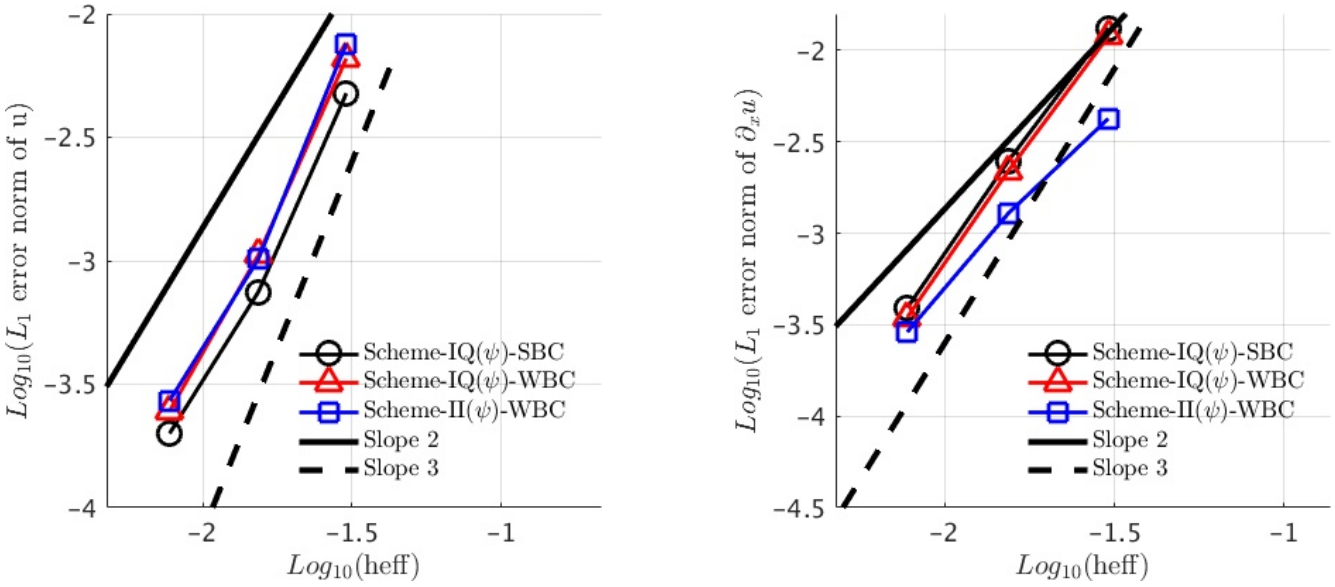

(a) Solution. (b) Gradient.

Figure 18: Error convergence results for the nonlinear problem.

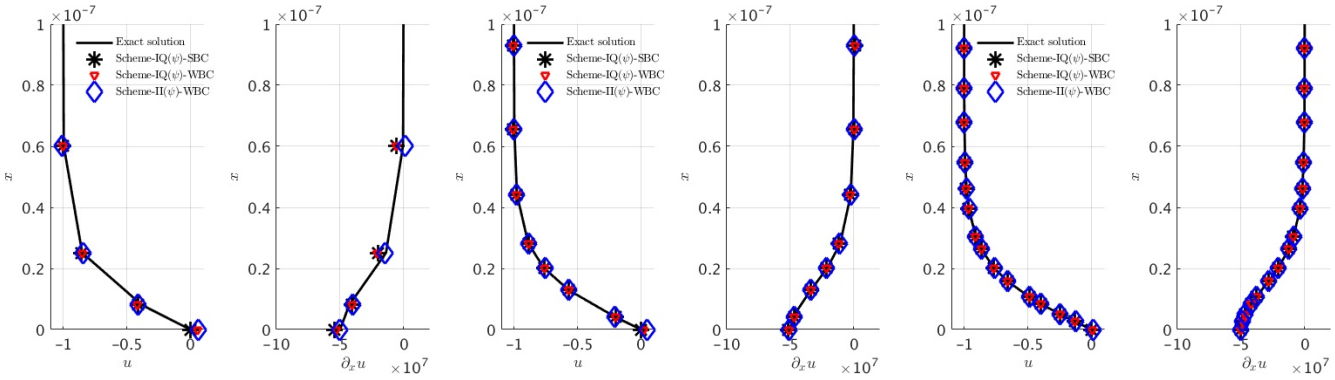

(a) Grid1: 32 nodes. (b) Grid2: 64 nodes. (c) Grid3: 128 nodes.

Figure 19: Solutions and gradients for the nonlinear problem.

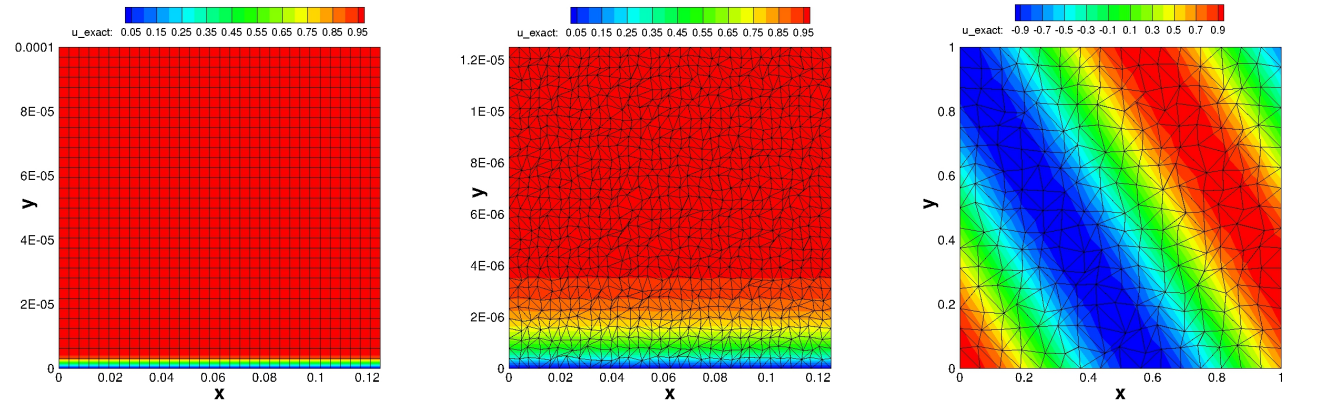

(a) Grid-SQ1: 33×33 nodes. (b) Grid-ST1: 33×33 nodes. (c) Grid-T1: 17×17 nodes.

Figure 20: Coarsest grids used in two-dimensional problems with exact solution contours.

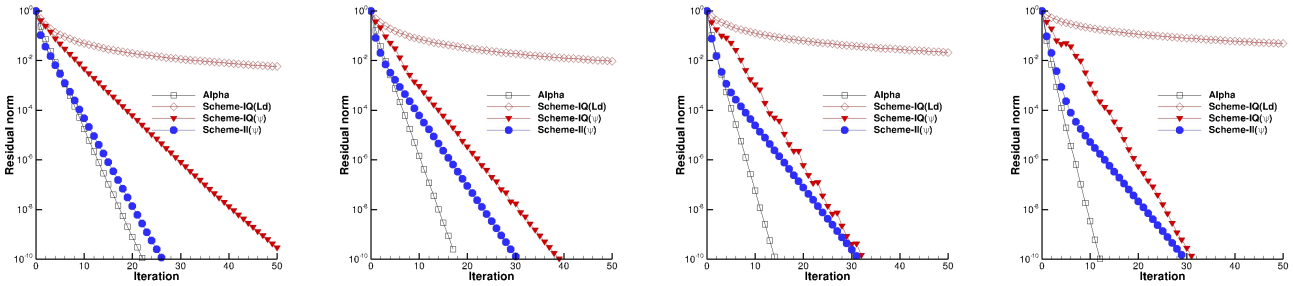

(a) Grid-SQ1. (b) Grid-SQ2. (c) Grid-SQ3. (d) Grid-SQ4.

Figure 21: Iterative convergence results for the two-dimensional boundary-layer problem on quadrilateral grids.

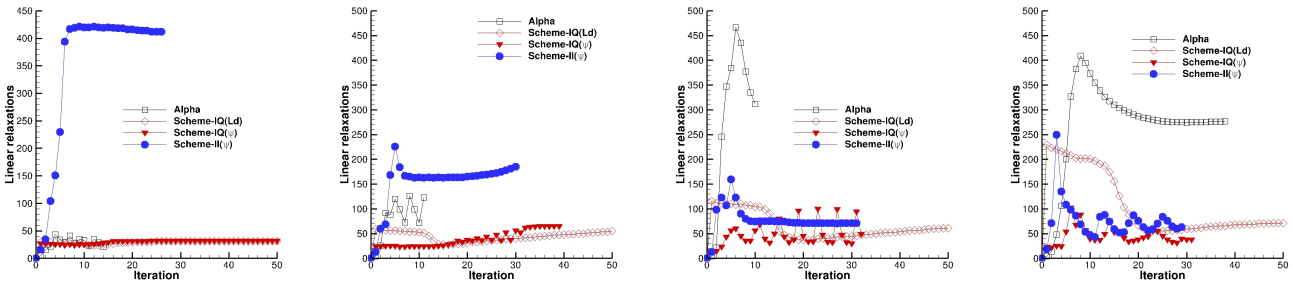

(a) Grid-SQ1. (b) Grid-SQ2. (c) Grid-SQ3. (d) Grid-SQ4.

Figure 22: The number of linear relaxations for the two-dimensional boundary-layer problem on quadrilateral grids.

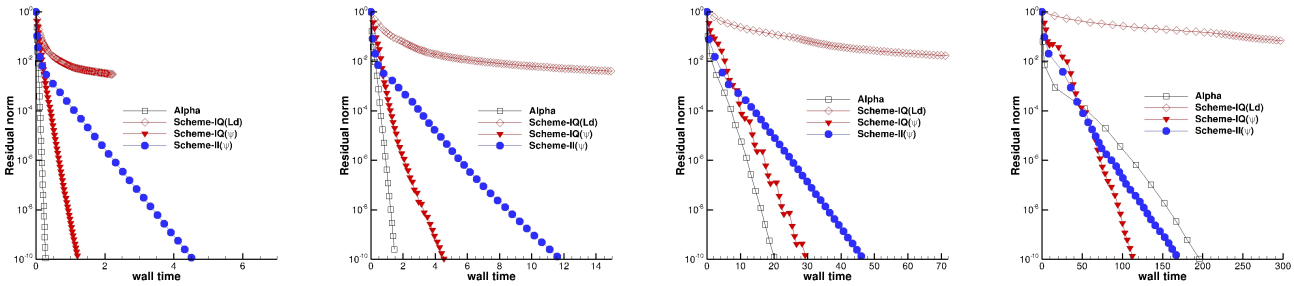

(a) Grid-SQ1. (b) Grid-SQ2. (c) Grid-SQ3. (d) Grid-SQ4.

Figure 23: Residual versus CPU time for the two-dimensional boundary-layer problem on quadrilateral grids.

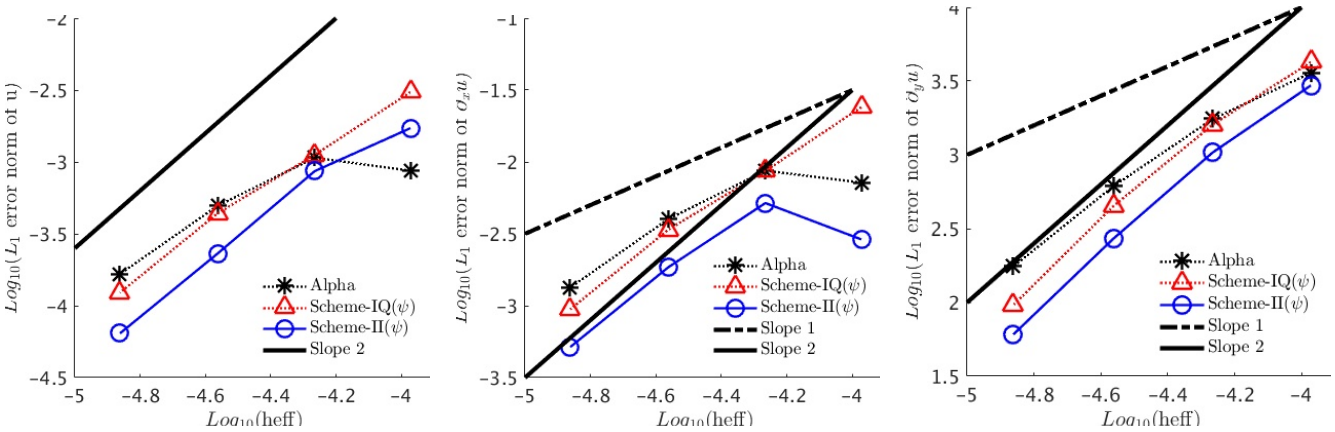

(a) Solution variable u. (b) Gradient $\partial_x u$. (c) Gradient $\partial_y u$.

Figure 24: Error convergence results for the two-dimensional boundary-layer problem on quadrilateral grids.

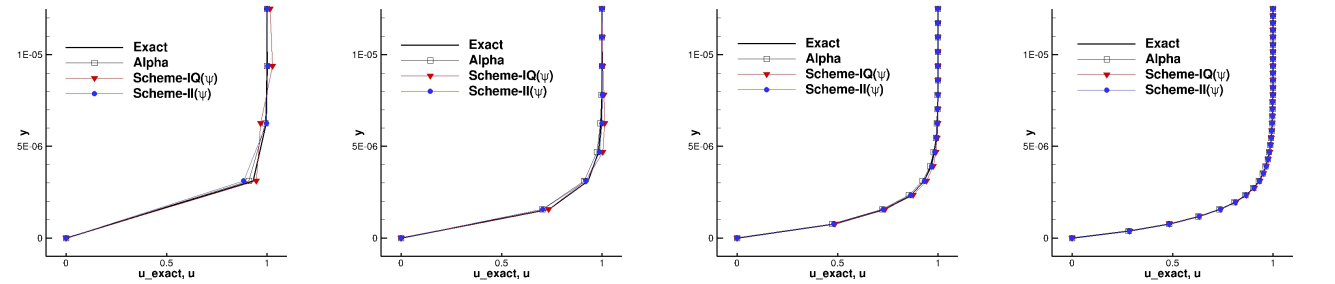

(a) Grid-SQ1. (b) Grid-SQ2. (c) Grid-SQ3. (d) Grid-SQ4.

Figure 25: Solution profiles at $x = 0.0625$ for the two-dimensional boundary-layer problem on quadrilateral grids.

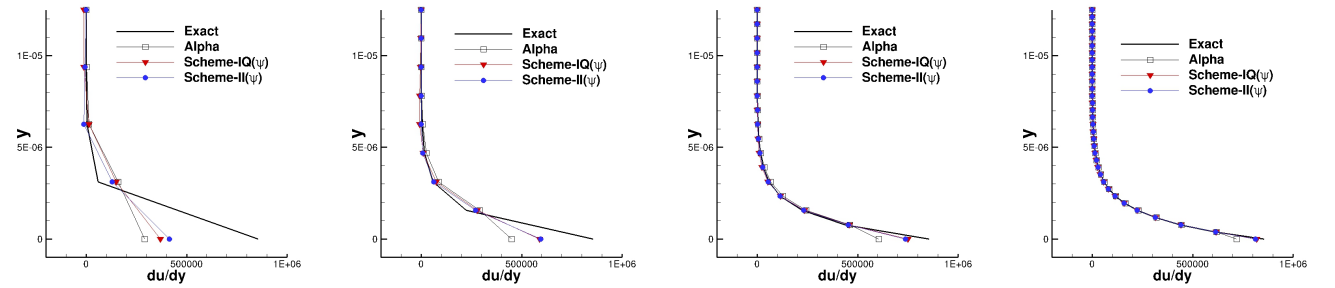

(a) Grid-SQ1. (b) Grid-SQ2. (c) Grid-SQ3. (d) Grid-SQ4.

Figure 26: Normal gradient profiles at $x = 0.0625$ for the two-dimensional boundary-layer problem on quadrilateral grids.

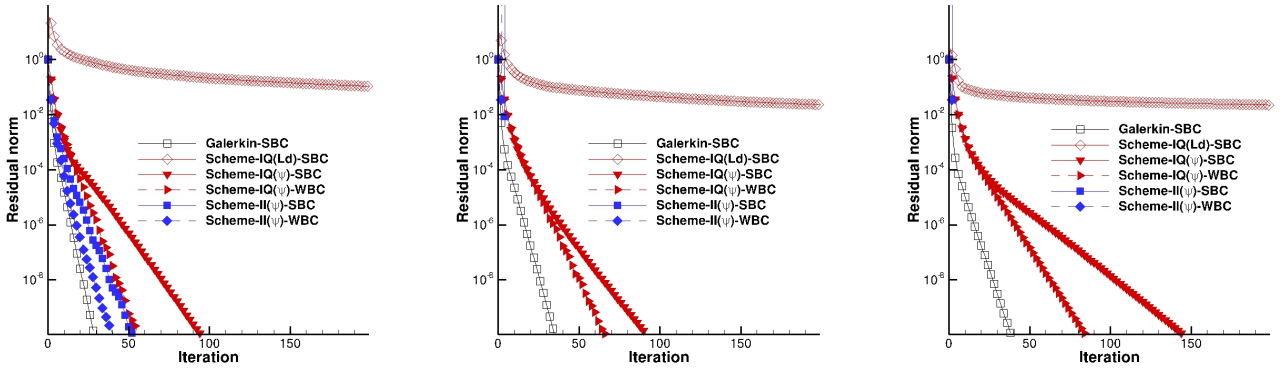

(a) Grid-ST1: Residual convergence. (b) Grid-ST2: Residual convergence. (c) Grid-ST3: Residual convergence.

Figure 27: Iterative convergence results for the two-dimensional boundary-layer problem on irregular triangular grids.

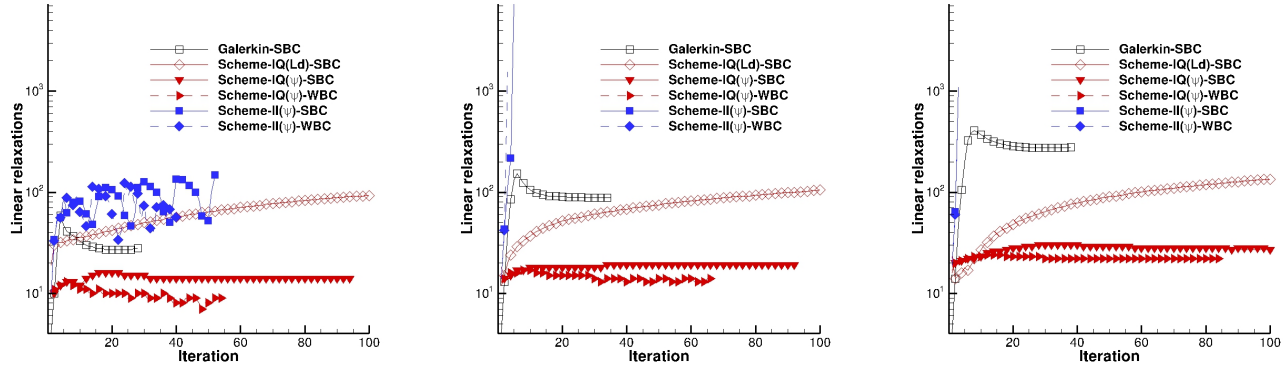

(a) Grid-ST1: Linear relaxations. (b) Grid-ST2: Linear relaxations. (c) Grid-ST3: Linear relaxations.

Figure 28: The number of linear relaxations for the two-dimensional boundary-layer problem on irregular triangular grids.

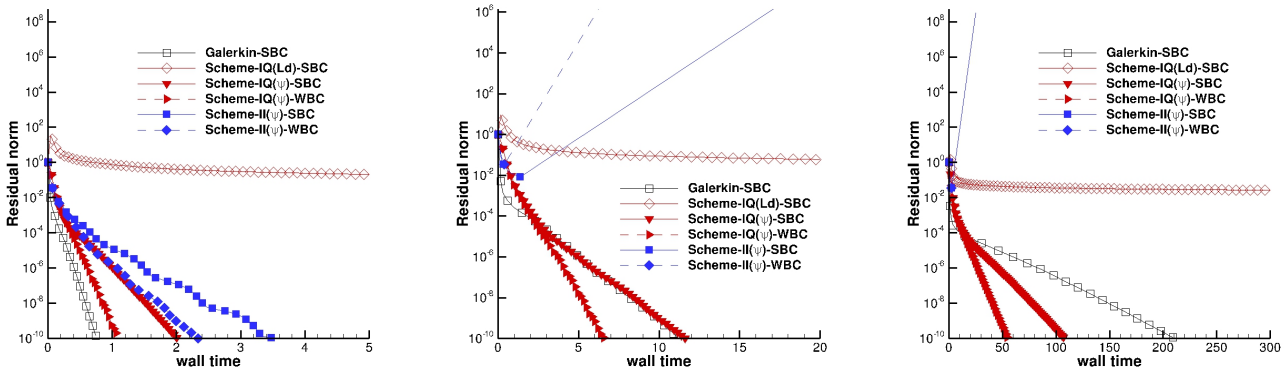

(a) Grid-ST1: CPU time. (b) Grid-ST2: CPU time. (c) Grid-ST3: CPU time.

Figure 29: Residual versus CPU time for the two-dimensional boundary-layer problem on irregular triangular grids.

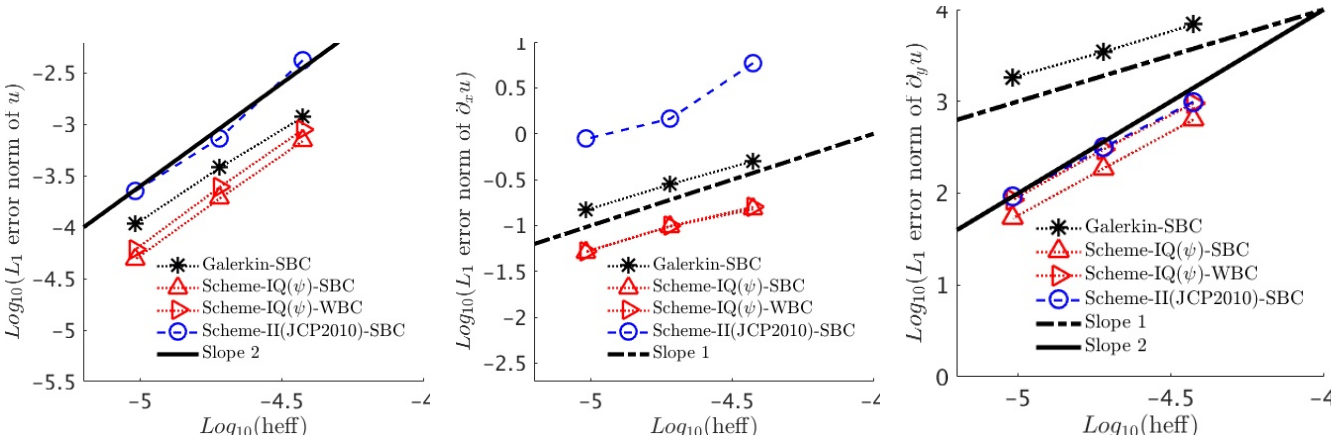

(a) Solution variable u. (b) Gradient $\partial_x u$. (c) Gradient $\partial_y u$.

Figure 30: Error convergence results for the two-dimensional boundary-layer problem on irregular triangular grids.

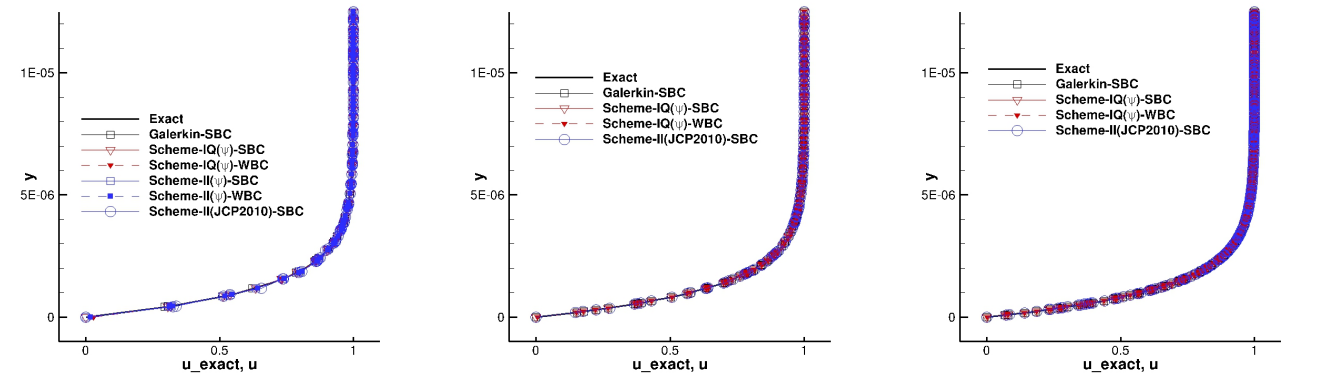

(a) Grid-ST1. (b) Grid-ST2. (c) Grid-ST3.

Figure 31: Solution profiles at $x = 0.0625$ for the two-dimensional boundary-layer problem on irregular triangular grids.

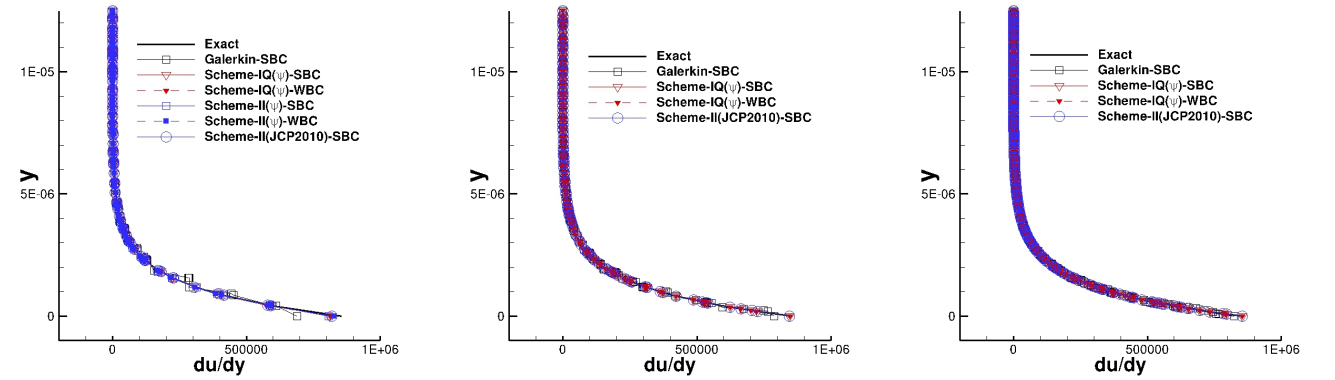

(a) Grid-ST1. (b) Grid-ST2. (c) Grid-ST3.

Figure 32: Normal gradient profiles at $x = 0.0625$ for the two-dimensional boundary-layer problem on irregular triangular grids.

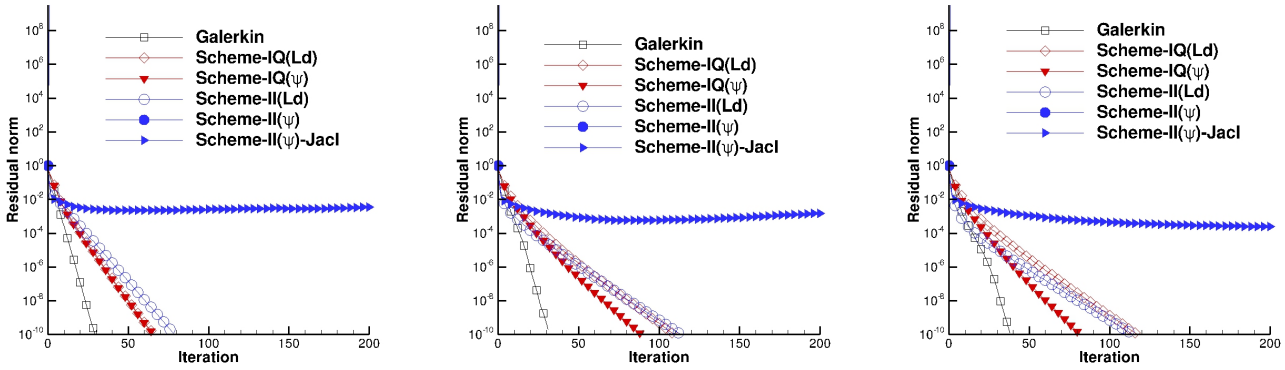

(a) Grid-T1. (b) Grid-T2. (c) Grid-T3.

Figure 33: Iterative convergence results for a two-dimensional problem with a smooth solution without a boundary layer.

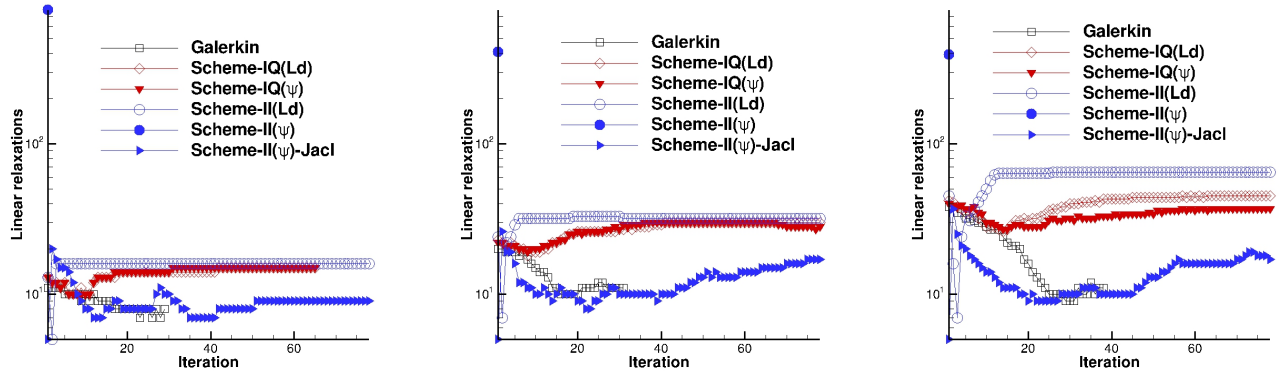

(a) Grid-T1: Linear relaxations. (b) Grid-T2: Linear relaxations. (c) Grid-T3: Linear relaxations.

Figure 34: The number of linear relaxations for a two-dimensional problem with a smooth solution without a boundary layer.

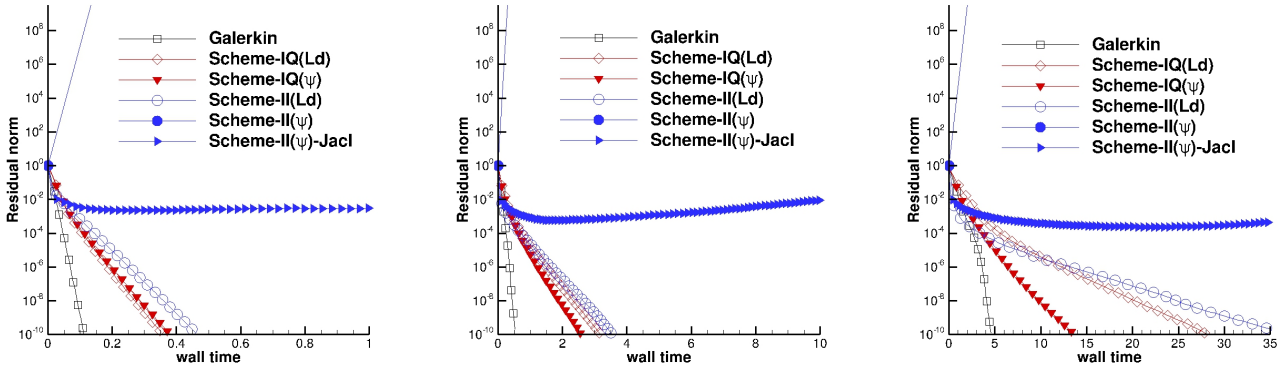

(a) Grid-T1. (b) Grid-T2. (c) Grid-T3.

Figure 35: Residual versus CPU time for a two-dimensional problem with a smooth solution without a boundary layer.

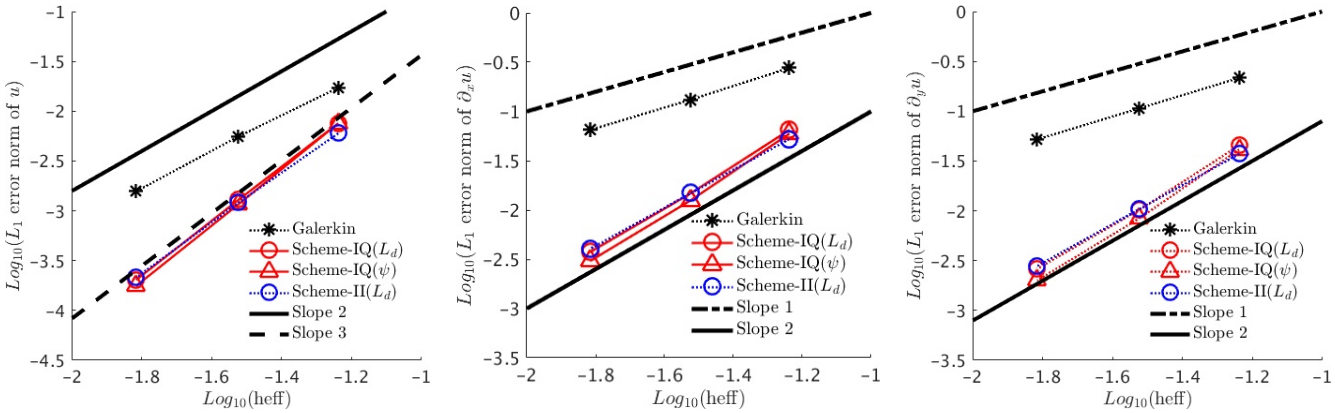

(a) Solution variable u. (b) Gradient $\partial_x u$. (c) Gradient $\partial_y u$.

Figure 36: Error convergence for a two-dimensional problem with a smooth solution without a boundary layer.

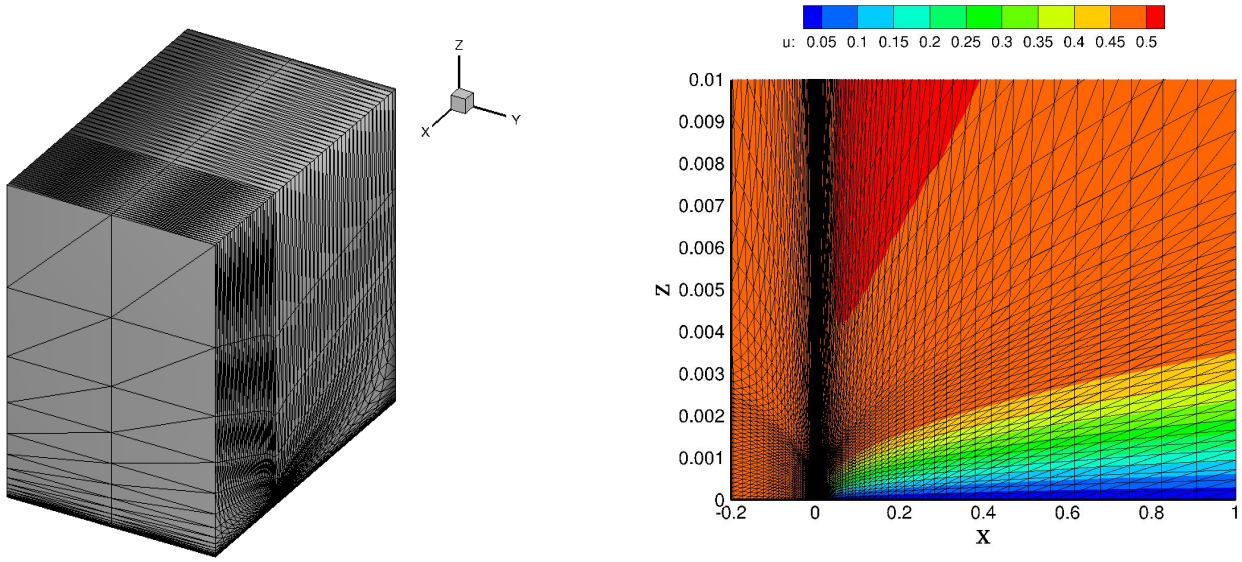

(a) 3D grid.

(b) Section at $y = 1.0$.

Figure 37: The coarsest grid used for a laminar flat plate case.

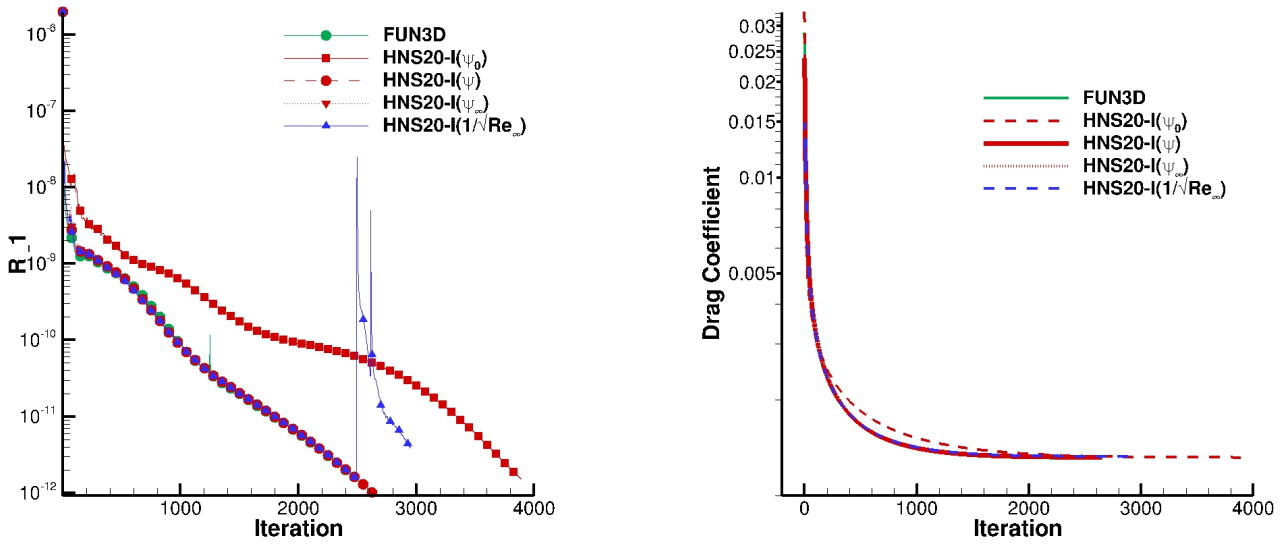

(a) Continuity residual convergence.

(b) Drag convergence.

Figure 38: Drag coefficient and residual convergence histories for the finest grid in a laminar flat plate case.

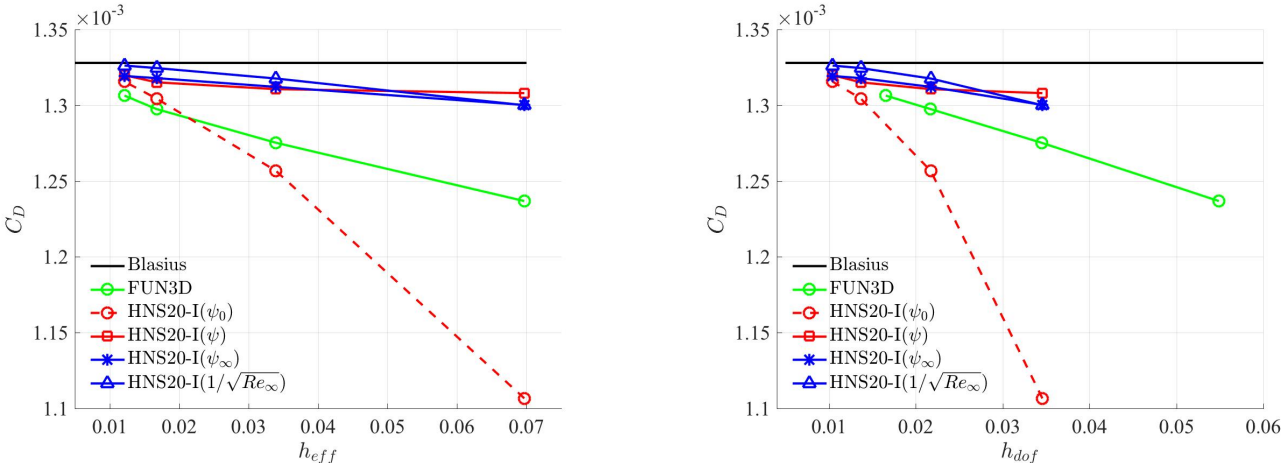

(a) C_D versus h_{eff}.

(b) C_D versus h_{dof}.

Figure 39: Drag coefficient convergence for a laminar flat plate case.

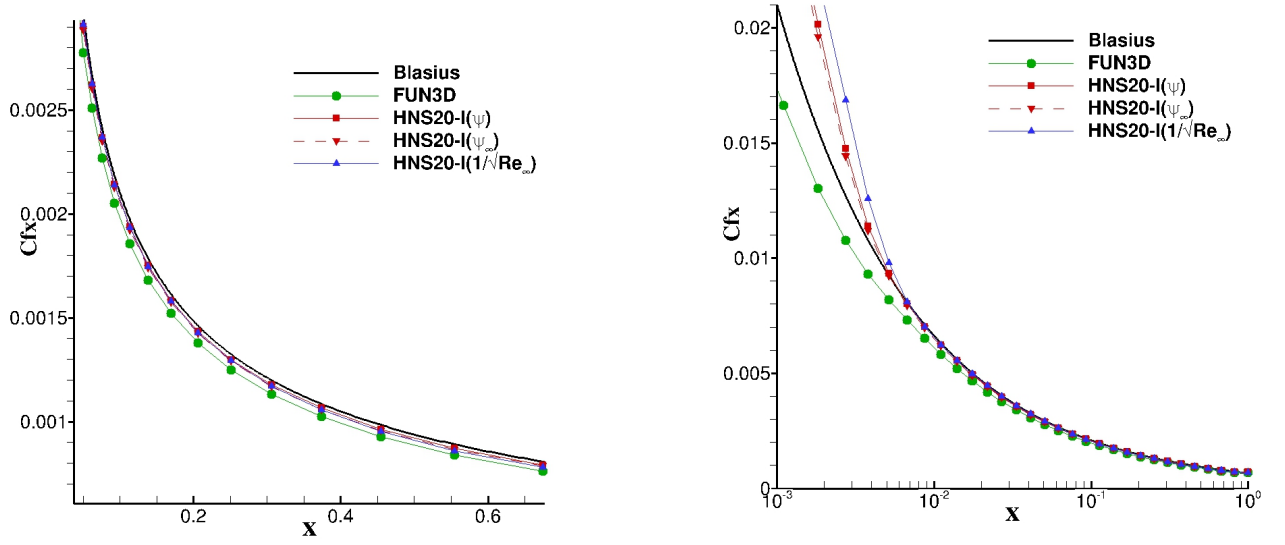

(a) Close view in the middle of the flat plate.

(b) Close view near the leading edge.

Figure 40: Skin friction distributions.

Appendix A: Boundary Condition for Hyperbolic Diffusion System

Consider the diffusion equation in $x \in (0,1)$:

$$0 = \partial_{xx} u + s(x), \tag{A.1}$$

where $s(x)$ is a source term. Integrating the equation twice, we obtain

$$u(x) = c_0 + c_1 x + \int \left(\int s(x)\, dx \right) dx, \tag{A.2}$$

where c_0 and c_1 are arbitrary constants. It shows that two boundary conditions are required to determine the solution, which can be imposed on u (Dirichlet) or $\partial_x u$ (Neumann) at $x = 0$ and $x = 1$.

Consider the hyperbolic diffusion system,

$$\partial_\tau u = \partial_x p + s(x), \tag{A.3}$$

$$\partial_\tau u = \frac{1}{T_r}(\partial_x u - p). \tag{A.4}$$

In the pseudo steady state, we have

$$0 = \partial_x p + s(x), \tag{A.5}$$

$$0 = \partial_x u - p. \tag{A.6}$$

Note that this is the system we discretize and define the residual in the hyperbolic method. The system is integrated just once to yield

$$p(x) = c_1 + \int s(x)\, dx, \tag{A.7}$$

$$u(x) = \int p\, dx = c_0 + c_1 x + \int \left(\int s(x)\, dx \right) dx. \tag{A.8}$$

Therefore, again, we have two arbitrary constants c_0 and c_1, and therefore only two boundary conditions are required to determine the solution. In effect, the second derivative term in the original diffusion equation is expressed as a set of two first-order equations; the former is integrated twice and the latter is integrated once for two equations, thus giving two arbitrary constants and thus requiring two boundary conditions in both cases. The hyperbolic formulation provides an additional insight that there is always one wave (in the pseudo-time characteristics) entering the domain at each boundary and therefore two boundary conditions are required [1]. Also, it simplifies the implementation of a Neumann condition as a specification of p at a boundary; in effect, a Neumann condition on u becomes a Dirichlet condition on p. It is emphasized that the first-order formulation with the auxiliary variable p does not change the physical problem, and so the boundary condition must not be changed.

Appendix B: Derivation of the Length Scale in AIAA2016-3969

The length scale proposed in Ref.[4] is derived as follows. Following Ref.[2], we derive T_r that will equalize the relaxation time scale T_r and the time scale of the *approximate* wave speed $|a| + a_v$, which characterizes the dissipation matrix (II.11) in the simplified approach:

$$T_r = \frac{\ell}{|a| + \sqrt{\nu / T_r}}, \tag{B.1}$$

where ℓ is a length scale to be defined. Note that in the unified approach [2], the true wave speed $a/2 + a/2\sqrt{1 + 4\nu/(T_r a^2)}$ is used to derive T_r. Solving Equation (B.1) for T_r, we obtain two solutions:

$$T_r = \frac{2\ell^2/\nu}{2|Re_\ell| + 1 \pm \sqrt{4\,|Re_\ell| + 1}}, \quad |Re_\ell| = \frac{|a|\ell}{\nu}. \tag{B.2}$$

The solution with the positive sign is useful because it allows us to express T_r in the form (II.4) with a positive length scale L_r:

$$T_r = \frac{L_r^2}{\nu}, \quad L_r = \frac{\ell}{1/2 + \sqrt{|Re_\ell| + 1/4}}. \tag{B.3}$$

It is instructive to look at its limits:

$$T_r \to \frac{\ell^2}{\nu} \qquad \text{as} \qquad |Re_\ell| \to 0, \tag{B.4}$$

$$T_r \to \frac{\ell}{a} \qquad \text{as} \qquad |Re_\ell| \to \infty, \tag{B.5}$$

which match the limits of the relaxation time defined for the unified hyperbolic system in Ref.[2]. It is thus reasonable to employ the length scale in Ref.[2] for ℓ:

$$\ell = \frac{1}{2\pi}\left[\frac{Re_\pi}{\sqrt{1+Re_\pi^2}+1} + \sqrt{1 + \frac{2}{\sqrt{1+Re_\pi^2}+1}}\,\right], \quad Re_\pi \equiv \frac{|a|(1/\pi)}{\nu}. \tag{B.6}$$

Then, the hyperbolic advection-diffusion system retains a full form in the balanced high-Reynolds-number limit:

$$\partial_\tau u + a\partial_x u = \partial_x p, \tag{B.7}$$

$$\partial_\tau p = \frac{1}{T_r}\left(\nu \partial_x u - p\right), \tag{B.8}$$

because T_r does not increase indefinitely as it does with $L_r = \frac{1}{2\pi}$, and stays finite as $\nu \to 0$ by Equation (B.3). However, this length scale does not fully resolve high-Reynolds-number issues for the model equations. As discussed in this paper, it is not T_r but a_v that needs to be finite to resolve the boundary layer issues; the length scale in Equation (B.3) leads to $a_v = O(1/\sqrt{Re}) \to 0$ as $Re \to \infty$. The success for the Navier-Stokes equations as reported in Ref.[4] has been found due to the use of the free stream Reynolds number with which it serves as an effective approximation as discussed in this paper. However, a similar approximate formula does not work well for the viscous Burgers equation.

Appendix C: Dissipation Matrix by Unified Advection-Diffusion Eigen-Structure

The upwind dissipation matrix $\mathbf{Q}$ in Equation (II.10) can be constructed based on the full eigen-structure of the hyperbolic advection-diffusion system (II.7). The hyperbolic formulation considered in this paper is similar to the one introduced in Ref.[5], and slightly different from that used in Ref.[2]. Also, here, we consider a more general case where a is allowed to be negative; Ref.[2] considers only positive values of a.

Consider the preconditioned flux Jacobian, which characterizes the wave structure of the hyperbolic advection-diffusion system:

$$\mathbf{PA} = \mathbf{P}\frac{\partial \mathbf{f}}{\partial \mathbf{u}} = \begin{bmatrix} a & -1 \\ -\nu/T_r & 0 \end{bmatrix}. \tag{C.1}$$

It has the following eigenvalues:

$$\lambda_1 = \frac{1}{2}\left[a - \sqrt{a^2 + \frac{4\nu}{T_r}}\,\right], \quad \lambda_2 = \frac{1}{2}\left[a + \sqrt{a^2 + \frac{4\nu}{T_r}}\,\right]. \tag{C.2}$$

These are exactly the same as those in Ref.[2], and thus T_r is derived in exactly the same way as described in Ref.[2] as

$$T_r = \frac{L_r}{|a| + a_v}, \tag{C.3}$$

where a_v represents the wave speed in the diffusion limit:

$$a_v = \frac{\nu}{L_r}, \tag{C.4}$$

so that, the eigenvalues are then expressed as

$$\lambda_1 = a^- - a_v \le 0, \quad \lambda_2 = a^+ + a_v \ge 0, \quad a^- = \min(0, a), \quad a^+ = \max(0, a). \tag{C.5}$$

The optimal relaxation length scale can also be derived in the same way as in Ref.[2]:

$$L_r = \frac{1}{2\pi}\left[\frac{Re_\pi}{\sqrt{1+Re_\pi^2}+1} + \sqrt{1+\frac{2}{\sqrt{1+Re_\pi^2}+1}}\ \right], \quad Re_\pi \equiv \frac{|a|(1/\pi)}{\nu}. \tag{C.6}$$

However, the right-eigenvectors are slightly different from those in Ref.[2]:

$$\mathbf{R} = \begin{bmatrix} 1 & 1 \\ \lambda_2 & \lambda_1 \end{bmatrix} = \begin{bmatrix} 1 & 1 \\ a^+ + a_v & a^- - a_v \end{bmatrix}. \tag{C.7}$$

The absolute Jacobian relevant to the construction of the upwind flux is obtained as

$$|\mathbf{PA}| = \mathbf{R}\begin{bmatrix} |\lambda_1| & 0 \\ 0 & |\lambda_2| \end{bmatrix}\mathbf{R}^{-1} = \begin{bmatrix} \dfrac{a_v\left(|Re_{L_r}|^2 + 2\,|Re_{L_r}| + 2\right)}{|Re_{L_r}|+2} & -\dfrac{Re_{L_r}}{|Re_{L_r}|+2} \\ -\dfrac{a_v^2 Re_{L_r}\left(|Re_{L_r}|+1\right)}{|Re_{L_r}|+2} & \dfrac{2a_v\left(|Re_{L_r}|+1\right)}{|Re_{L_r}|+2} \end{bmatrix}, \tag{C.8}$$

where

$$Re_{L_r} = \frac{aL_r}{\nu} = \frac{a}{a_v}, \quad |Re_{L_r}| = \frac{|a|L_r}{\nu} = \frac{|a|}{a_v}. \tag{C.9}$$

The upwind flux is constructed as

$$\Phi(\mathbf{u}_L, \mathbf{u}_R) = \frac{1}{2}\left(\mathbf{f}_L + \mathbf{f}_R\right) - \frac{1}{2}\mathbf{P}^{-1}\,|\mathbf{PA}|\,(\mathbf{u}_R - \mathbf{u}_L), \tag{C.10}$$

and therefore, the dissipation matrix $\mathbf{Q}$ is given by

$$\mathbf{Q} = \mathbf{P}^{-1}\,|\mathbf{PA}|, \tag{C.11}$$

which is positive definite by construction. This is the dissipation matrix used for Scheme-II(JCP2010) in Section VI.A.2.

In two dimensions, we consider the following formulation:

$$\partial_\tau u + a\partial_x u + b\partial_y u = \nu(\partial_x p + \partial_x q), \quad T_r\partial_\tau p = \partial_x u - p, \quad T_r\partial_\tau p = \partial_y u - q, \tag{C.12}$$

or in the vector form,

$$\mathbf{P}^{-1}\partial_\tau \mathbf{u} + \partial_x \mathbf{f} + \partial_y \mathbf{g} = \mathbf{s}, \tag{C.13}$$

where

$$\mathbf{P}^{-1} = \begin{bmatrix} 1 & 0 & 0 \\ 0 & T_r & 0 \\ 0 & 0 & T_r \end{bmatrix}, \mathbf{u} = \begin{bmatrix} u \\ p \\ q \end{bmatrix}, \quad \mathbf{f} = \begin{bmatrix} au - \nu p \\ -1 \\ 0 \end{bmatrix}, \quad \mathbf{g} = \begin{bmatrix} bu - \nu q \\ 0 \\ -1 \end{bmatrix}, \quad \mathbf{s} = \begin{bmatrix} 0 \\ -p \\ -q \end{bmatrix}. \tag{C.14}$$

The flux Jacobian that characterizes the wave structure is

$$\mathbf{PA} = \mathbf{P}\left(\frac{\partial \mathbf{f}}{\partial \mathbf{u}}n_x + \frac{\partial \mathbf{g}}{\partial \mathbf{u}}n_y\right) = \begin{bmatrix} a_n & -\nu n_x & -\nu n_y \\ -n_x/T_r & 0 & 0 \\ -n_y/T_r & 0 & 0 \end{bmatrix}, \tag{C.15}$$

where $a_n = an_x + bn_y$, and $\mathbf{n} = (n_x, n_y)$ is an arbitrary unit vector, which is taken as the face normal for a numerical flux. This matrix is identical to the one considered in Ref.[2]. Following Ref.[2], we define T_r as

$$T_r = \frac{L_r}{|a_n| + \nu/L_r}, \tag{C.16}$$

with L_r given by Equation (C.6), and thus the eigenvalues of $\mathbf{PA}$ are given by

$$\lambda_1 = a_n^- - a_v, \quad \lambda_2 = a_n^+ + a_v, \quad \lambda_3 = 0, \tag{C.17}$$

where $a_v = \nu/L_r$.

$$a_n^- = \min(0, a_n), \quad a_n^+ = \max(0, a_n), \quad a_v = \nu/L_r. \tag{C.18}$$

The right and left eigenvector matrices are given by

$$\mathbf{R} = \begin{bmatrix} \dfrac{L_r}{Re_{L_r}^+ + 1} & \dfrac{L_r}{Re_{L_r}^- - 1} & 0 \\ n_x & n_x & -n_y \\ n_y & n_y & n_x \end{bmatrix}, \tag{C.19}$$

$$\mathbf{L} = \mathbf{R}^{-1} = \begin{bmatrix} \dfrac{|Re_{L_r}| + 1}{L_r(|Re_{L_r}| + 2)} & \dfrac{(Re_{L_r}^+ + 1)n_x}{|Re_{L_r}| + 2} & \dfrac{(Re_{L_r}^+ + 1)n_y}{|Re_{L_r}| + 2} \\ -\dfrac{|Re_{L_r}| + 1}{L_r(|Re_{L_r}| + 2)} & \dfrac{(1 - Re_{L_r}^-)n_x}{|Re_{L_r}| + 2} & \dfrac{(1 - Re_{L_r}^-)n_y}{|Re_{L_r}| + 2} \\ 0 & -n_y & n_x \end{bmatrix}, \tag{C.20}$$

where

$$Re_{L_r} = \frac{a_n L_r}{\nu}, \quad |Re_{L_r}| = \frac{|a_n| L_r}{\nu}, \quad Re_{L_r}^- = \frac{a_n^- L_r}{\nu}, \quad Re_{L_r}^+ = \frac{a_n^+ L_r}{\nu}. \tag{C.21}$$

Note that the matrix $\mathbf{L}$ given in Ref.[2] has a wrong factor in the last row; it is corrected in the above. The absolute Jacobian that defines the dissipation matrix is given by

$$|\mathbf{PA}| = \mathbf{R} \begin{bmatrix} |\lambda_1| & 0 & 0 \\ 0 & |\lambda_2| & 0 \\ 0 & 0 & 0 \end{bmatrix} \mathbf{R}^{-1} \tag{C.22}$$

$$= a_v \frac{|Re_{L_r}| + 1}{|Re_{L_r}| + 2} \begin{bmatrix} |Re_{L_r}| + 1 + \dfrac{1}{|Re_{L_r}| + 1} & -\dfrac{L_r Re_{L_r} n_x}{|Re_{L_r}| + 1} & -\dfrac{L_r Re_{L_r} n_y}{|Re_{L_r}| + 1} \\ -\dfrac{Re_{L_r} n_x}{L_r} & 2n_x^2 & 2n_x n_y \\ -\dfrac{Re_{L_r} n_y}{L_r} & 2n_x n_y & 2n_y^2 \end{bmatrix}. \tag{C.23}$$

The upwind flux is constructed as

$$\Phi(\mathbf{u}_L, \mathbf{u}_R) = \frac{1}{2}\left((\mathbf{f}_L, \mathbf{g}_L) + (\mathbf{f}_R, \mathbf{g}_R)\right) \cdot \mathbf{n} - \frac{1}{2}\mathbf{P}^{-1}\left|\mathbf{PA}\right|\left(\mathbf{u}_R - \mathbf{u}_L\right), \tag{C.24}$$

and therefore, the dissipation matrix $\mathbf{Q}$ is given by

$$\mathbf{Q} = \mathbf{P}^{-1}\left|\mathbf{PA}\right|, \tag{C.25}$$

which is positive definite by construction. This is the dissipation matrix used for Scheme-II(JCP2010) in Section VI.A.2.

The unified approach allows a systematic and straightforward construction of numerical schemes for the hyperbolic advection-diffusion system. As demonstrated in this paper, the resulting scheme yields accurate solutions to boundary-layer problems; no modifications are necessary in the length scale L_r. However, it is very difficult to

extend it to complex systems such as the Navier-Stokes equations. Eigenvalues for the hyperbolic Navier-Stokes system as a unified system have not been found yet in a closed form although the hyperbolicity has been claimed in one dimension in Ref.[27]. In contrast, the simplified approach considered in this paper, where the upwind numerical flux is constructed simply as a sum of the upwind advection scheme and the upwind hyperbolic diffusion scheme, requires a proof of hyperbolicity only for the viscous terms, which has been provided in Ref.[3] for the three-dimensional compressible Navier-Stokes equations. The simplified approach, however, requires a modification of the relaxation length scale for high-Reynolds-number boundary-layer problems as discussed in this paper.